Mitophagy regulates integrity of mitochondria at synapses and is critical for synaptic maintenance

Sinsuk Han[†], Yu Young Jeong[†] ID, Preethi Sheshadri, Xiao Su & Qian Cai* ID

Abstract

Synaptic mitochondria are particularly vulnerable to physiological insults, and defects in synaptic mitochondria are linked to early pathophysiology of Alzheimer's disease (AD). Mitophagy, a cargo-specific autophagy for elimination of dysfunctional mitochondria, constitutes a key quality control mechanism. However, how mitophagy ensures synaptic mitochondrial integrity remains largely unknown. Here, we reveal Rheb and Snapin as key players regulating mitochondrial homeostasis at synapses. Rheb initiates mitophagy to target damaged mitochondria for autophagy, whereas dynein–Snapin-mediated retrograde transport promotes clearance of mitophagosomes from synaptic terminals. We demonstrate that synaptic accumulation of mitophagosomes is a feature in AD-related mutant hAPP mouse brains, which is attributed to increased mitophagy initiation coupled with impaired removal of mitophagosomes from AD synapses due to defective retrograde transport. Furthermore, while deficiency in dynein–Snapin-mediated retrograde transport recapitulates synaptic mitophagy stress and induces synaptic degeneration, elevated Snapin expression attenuates mitochondrial defects and ameliorates synapse loss in AD mouse brains. Taken together, our study provides new insights into mitophagy regulation of synaptic mitochondrial integrity, establishing a foundation for mitigating AD-associated mitochondria deficits and synaptic damage through mitophagy enhancement.

Introduction

Neurons have high and continuous energy demands in order to maintain their proper function. Mitochondria are the main cellular energy powerhouses, supplying most of ATP by oxidative phosphorylation (OXPHOS), which is required to fuel critical neuronal functions (Sheng & Cai, 2012; Cai & Tammineni, 2016, 2017; Chamberlain & Sheng, 2019). Mitochondria also enact essential reactions of metabolism and Ca^{2+} signaling, as well as regulate cellular life/death decisions. Aged and malfunctioning mitochondria are defective in energy production and Ca^{2+} buffering, and also release reactive oxygen species (ROS) that are harmful at high concentrations. These defects compromise support in synaptic activities (Reddy et al, 2010; Reddy, 2011; Sheng & Cai, 2012; Cai & Tammineni, 2017). Thus, it is not unexpected that volumes of evidence suggest that mitochondrial dysfunction underlies cognitive impairment in neuronal aging and is one of the most notable hallmarks of age-related neurodegenerative diseases. Importantly, the earliest features of the onset of the highly prevalent Alzheimer's disease (AD) have been linked to mitochondrial pathology—abnormal accumulation of damaged mitochondria (Gibson & Shi, 2010; Swerdlow et al, 2010; Cai & Tammineni, 2016; Reddy & Oliver, 2019). Mitochondrial quality control, then, emerges as a central problem in the most common neurodegenerative disorders and is a clear target point for early interference in disease. Mitophagy, a specialized form of autophagy, constitutes a key mitochondrial quality control mechanism involving sequestration of damaged mitochondria into autophagosomes for subsequent degradation within lysosomes (Youle & Narendra, 2011; Sheng & Cai, 2012; Cai & Tammineni, 2016; Pickles et al, 2018). Even though some unique features of mitophagy in neurons have been described, mechanistic understanding of neuronal mitophagy and its link to pathological conditions remains very limited. Autophagocytosis of mitochondria in neurons was shown to be a feature in AD patient brains (Moreira et al, 2007a,b). Mitophagic abnormalities in AD have been demonstrated in a number of recent studies (Ye et al, 2015; Du et al, 2017; Manczak et al, 2018; Reddy et al, 2018; Cummins et al, 2019; Fang et al, 2019). Moreover, mitophagy stimulation was shown to abolish AD pathology and reverse memory impairment in AD models (Du et al, 2017; Fang et al, 2019). Therefore, there is an urgent need to investigate the detailed interaction between mitophagy deregulation and AD-linked pathological processes.

Healthy mitochondria must function at synapses for neurotransmission. It has been well established that mitochondria-mediated ATP supply and Ca^{2+} buffering sustain various essential functions at synaptic sites (Manji et al, 2012; Sheng & Cai, 2012). However, the mechanism underlying mitochondrial maintenance at synaptic

Division of Life Science, Department of Cell Biology and Neuroscience, School of Arts and Sciences, Rutgers, The State University of New Jersey, Piscataway, NJ, USA
*Corresponding author. Tel: +1 848 445 1633; E-mail: cai@biology.rutgers.edu
[†]These authors contributed equally to this work

terminals is understudied in neurobiology. A major gap in our understanding is whether mitophagy serves as a key player to ensure mitochondrial integrity and function at synapses, crucial for the support of synaptic activities. Early deficit in synaptic mitochondria has been implicated in the development of synaptic pathology in AD (Reddy & Beal, 2008; Du *et al*, 2010, 2012; Reddy, 2011; Cai & Tammineni, 2017; Guo *et al*, 2017). Synaptic mitochondria are more susceptible to amyloid β (Aβ)-induced damage and display early and significant accumulation of Aβ in AD brains before extensive extracellular Aβ deposition (Reddy & Beal, 2008; Du *et al*, 2012; Cai & Tammineni, 2017). Early-impacted mitochondria underwent declines in respiration, complex IV activity, and Ca^{2+} handling capacity, as well as elevated ROS production and enhanced probability of mitochondrial permeability transition pore (MPTP) (Reddy & Beal, 2008; Reddy *et al*, 2010; Reddy, 2011; Du *et al*, 2012; Cai & Tammineni, 2017; Tonnies & Trushina, 2017). This raises an important question as to whether synaptic mitochondrial deficit is attributed to impaired mitochondrial maintenance as a result of defects in removal of damaged mitochondria from AD synapses.

In the current study, we reveal that small GTPase Ras homolog enriched in brains (Rheb) initiates mitophagy and coordinates with dynein–Snapin-mediated retrograde transport, thus regulating the integrity of synaptic mitochondria. Rheb facilitates autophagic recruitment of damaged mitochondria to form mitophagosomes in distal axons, whereas dynein–Snapin-mediated retrograde transport removes nascent mitophagosomes and thus reduces mitochondrial stress at synaptic terminals. Furthermore, our studies uncover that AD-related mutant hAPP mouse brains exhibit robust presynaptic retention of mitophagosomes. Such a defect is caused by increased mitophagy initiation and impaired retrograde transport of mitophagosomes. Ablation of *snapin* in mouse brains mimics AD-associated synaptic mitophagy stress accompanied by synaptic degeneration. In contrast, Snapin-enhanced retrograde transport attenuates synaptic mitochondrial defects through promoting removal of axonal mitophagosomes, thereby ameliorating synapse loss in AD mouse brains. Therefore, our findings provide new insights into the involvement of mitophagy failure in synaptic mitochondrial deficits and thus advance our understanding of the mechanisms underlying AD-linked synaptic deterioration, one of the earliest pathologies in stricken neurons.

Results

Rheb initiates mitophagy within axons upon mitochondrial damage

We determined whether mitophagy is critical for maintaining mitochondrial integrity in the axons of neurons. Rheb was previously reported to be associated with mitochondria and promote autophagic engulfment of mitochondria in HeLa and muscle cells (Melser *et al*, 2013, 2015). We first examined whether Rheb is involved in autophagic removal of damaged mitochondria within axons. We conducted time-lapse imaging in live mature cortical neurons treated with CCCP, a mitochondrial membrane potential ($\Delta\psi_m$) uncoupler. Under basal conditions, Rheb is mainly present in the cytoplasm of axons and displays limited association with mitochondria. Strikingly, CCCP treatment induces robust Rheb localization to depolarized mitochondria. Rheb-associated mitochondria exhibit dominant retrograde movement along axons (anterograde, $2.51\% \pm 0.82\%$; retrograde, $29.88\% \pm 2.37\%$) (Fig 1A–C). Time-lapse images have shown that Rheb co-localizes and co-migrates with mitochondria along axons treated with CCCP. Interestingly, Rheb-tagged mitochondria exhibit high motility and move exclusively in a retrograde direction (Fig 1A and B). Consistent with our previous studies (Cai *et al*, 2012b; Ye *et al*, 2015; Lin *et al*, 2017), CCCP treatment remarkably reduces anterograde transport, but increases retrograde transport, of mitochondria along axons (anterograde, DMSO: $24.51\% \pm 2.25\%$; CCCP: $7.66\% \pm 1.42\%$; $P < 0.001$; retrograde, DMSO: $13.82\% \pm 1.23\%$; CCCP: $25.72\% \pm 1.65\%$; $P < 0.001$) (Fig EV1A and B). It is known that Parkin-mediated mitophagy induction leads to decreased anterograde transport of mitochondria. This is caused by Parkin-triggered and ubiquitin–proteasome system (UPS)-mediated degradation of mitochondrial Rho GTPase (Miro), a component of the adaptor–motor complex essential for KIF5 motors to drive anterograde transport of mitochondria in axons (Chan & Chan, 2011; Wang *et al*, 2011; Liu *et al*, 2012; Bingol *et al*, 2014; Birsa *et al*, 2014). We hypothesize that enhanced retrograde transport could be attributed to activation of Rheb-dependent mitophagy.

$\Delta\psi_m$ dissipation leads to increased percentage of mitochondria targeted by Rheb (DMSO: $14.53\% \pm 1.21\%$; CCCP: $35.24\% \pm 1.91\%$, $P < 0.001$) (Fig 1D and E). Alternatively, we examined the

---

Figure 1. Rheb initiates mitophagy within axons upon mitochondrial damage.

A–C Representative dual-channel kymographs (A) and quantitative analysis (C) showing that Rheb is recruited to mitochondria in axons and co-migrates with mitochondria in a predominant retrograde direction upon mitochondrial membrane potential ($\Delta\psi_m$) dissipation. The motility of mitochondria (Mito) and Rheb-associated mitochondria (Rheb-Mito) in axons was quantified, respectively. Vertical lines represent stationary organelles. Slanted lines or curves to the right (negative slope) represent anterograde movement; those to the left (positive slope) indicate retrograde movement. An organelle was considered stationary if it remained immotile (displacement ≤ 5 μm). Time-lapse images (B) showing co-localization and comigration (white arrows) of Rheb with mitochondria in a retrograde direction along axons during a 148-s recording period. Cortical neurons were transfected with GFP-Rheb and DsRed-Mito at 5–7 DIV and incubated with DMSO or 10 μM CCCP for 24 h prior to imaging at 10–12 DIV.

D, E Quantitative analysis (D) and representative images (E) showing robust association of Rheb with depolarized mitochondria within axons treated with CCCP. Rheb-SSVM, a farnesylation-deficient mutant of Rheb, fails to be recruited to mitochondria upon dissipating $\Delta\psi_m$. Mitochondria associated with Rheb were marked by white arrows. The percentages of mitochondria targeted by Rheb or Rheb-SSVM in the presence or absence of CCCP were quantified, respectively (D).

F–H Representative dual-channel kymographs (F) and quantitative analysis (G, H) showing that Rheb-mediated mitophagy activation depends on Rheb recruitment to mitochondria through Rheb farnesylation. Note that Rheb, but not Rheb-SSVM, is associated with autophagic vacuoles (AVs) within axons upon $\Delta\psi_m$ dissipation. Rheb-associated AVs move mainly in a retrograde direction along axons. The number of Rheb-associated AVs (Rheb-AVs) with or without CCCP treatment and the relative motilities of AVs and Rheb-AVs in CCCP-treated axons were quantified, respectively (G, H).

Data information: Data were quantified from the total number of neurons (n) indicated in parentheses (D, G) from greater than four experiments. Scale bars: 10 μm. Error bars represent SEM. Student's t-test: ***$P < 0.001$.
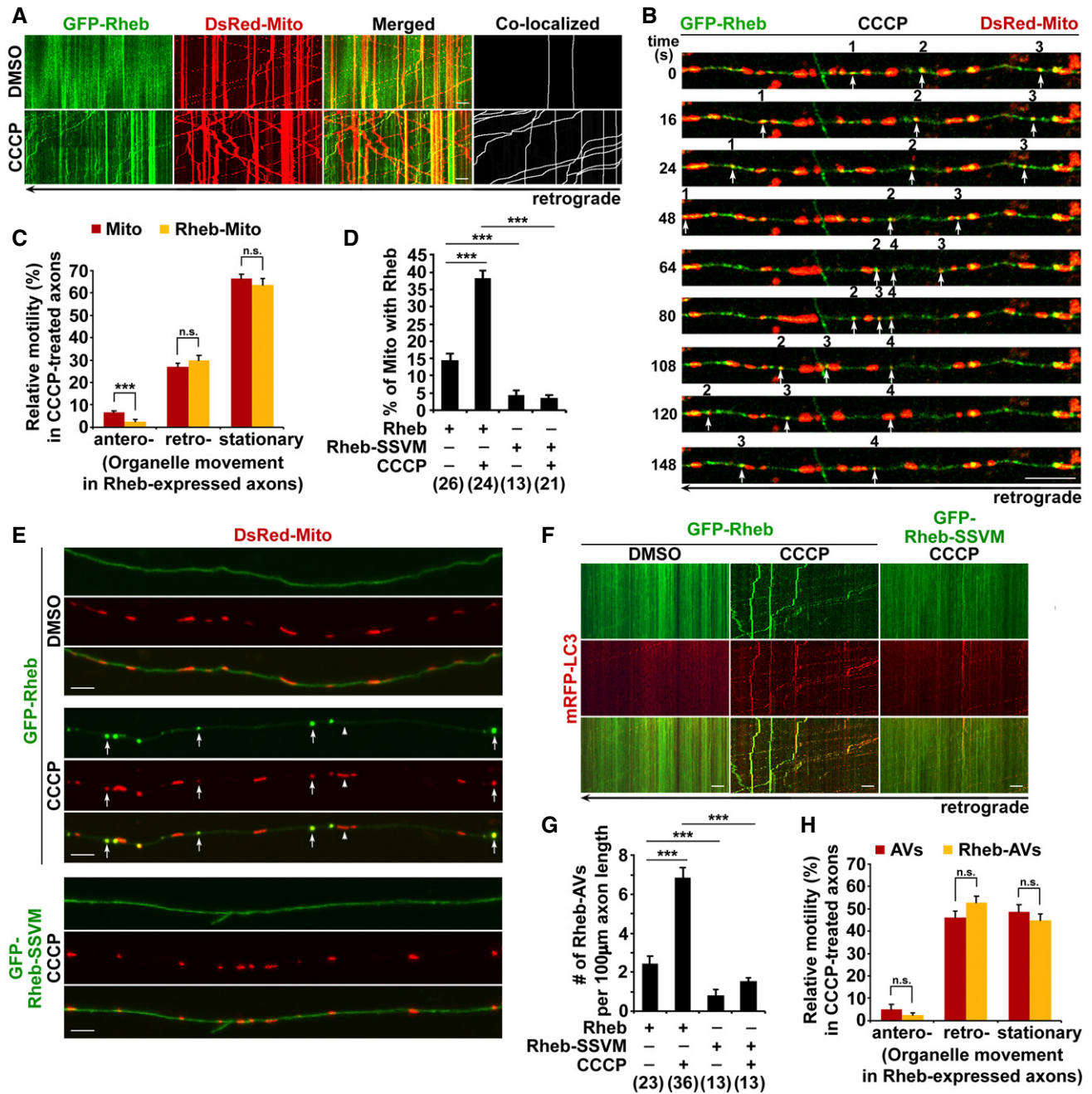
Figure 1.

effects of antimycin A (AA), a mitochondrial electron transport chain complex III inhibitor. Our previous studies have shown that a low concentration (1 μM) of AA in neurons depolarizes $\Delta\psi_m$, which is coupled with decreased mitochondrial respiration (Cai *et al*, 2012b; Lin *et al*, 2017). In the current study, AA treatment leads to a significant increase in Rheb localization to depolarized mitochondria within axons (40.59% ± 1.98%) (Fig EV1C and D), a finding consistent with our observation in CCCP-treated axons (Fig 1D and E). Furthermore, we did not observe enhanced mitochondrial association with Rheb-SSVM (Rheb-SSVM: 3.46% ± 0.87%, *P* < 0.001), a farnesylation-deficient mutant of Rheb (Basso *et al*, 2005). Thus,

our data suggest that Rheb is recruited to depolarized mitochondria in axons, which is dependent on Rheb farnesylation.

We have provided additional evidence showing that Rheb is associated with autophagic vacuoles (AVs), and CCCP treatment significantly increases the number of Rheb-associated AVs (Rheb-AVs) within axons (DMSO: 2.46 ± 0.35; CCCP: 6.86 ± 0.53; *P* < 0.001) (Fig 1F–H). Similar to AVs, these Rheb-AVs exhibit robust retrograde movement along axons. Our triple-channel image data further demonstrated that Rheb-associated AVs in axons contain engulfed mitochondria, suggesting that they are mitophagosomes in nature (Fig EV1E). In contrast, the same treatment fails to

increase the number of Rheb-SSVM-associated AVs (1.53 ± 0.19; Fig 1F and G), suggesting that Rheb localization to mitochondria is an essential step to initiate mitophagy in axons. Our data are consistent with previous studies showing that autophagosomes containing mitochondria move in a retrograde direction along axons (Maday *et al*, 2012; Wong & Holzbaur, 2014). This supports the possibility that mitophagy plays a role in regulating proper turnover of axonal mitochondria.

Our previous studies reported that nascent autophagosomes recruit dynein–Snapin, a motor–adaptor complex, to gain retrograde transport motility through fusion with late endosomes (LEs) to form amphisomes. Such a mechanism facilitates removal of AVs from distal axons for lysosomal degradation in the soma (Cheng *et al*, 2015a,b). Interestingly, Rheb-associated mitophagosomes are mostly positive for Rab7, a LE/amphisome marker (Fig EV1F). These data suggest that newly generated mitophagosomes fuse rapidly with LEs to form amphi-mitophagosomes, through which nascent mitophagosomes are loaded with dynein–Snapin transport machinery to enable retrograde transport motility. This result allows us to propose that Rheb-dependent mitophagy initiation coordinates with dynein–Snapin-mediated retrograde transport to remove damaged mitochondria from axonal terminals.

Rheb-mediated mitophagy in axons requires Nix but not Parkin

Next, we examined whether Rheb-associated mitophagy requires Nix, an outer mitochondrial membrane protein (Youle & Narendra, 2011; Cai & Jeong, 2020). Utilizing Nix shRNA that was previously described (Fei *et al*, 2004; Melser *et al*, 2013), we found that Nix RNAi results in markedly reduced localization of Rheb to axonal mitochondria upon $\Delta\psi_m$ dissipation (Scrambled shRNA: $38.83\% \pm 1.34\%$; Nix shRNA: $23.31\% \pm 1.26\%$; $P < 0.001$; Fig EV1G and H). Furthermore, Rheb-mediated autophagic targeting of mitochondria is impaired in axons expressing Nix shRNA, as evidenced by decreased number of Rheb-AVs (Scrambled shRNA: 8.99 ± 0.61; Nix shRNA: 1.92 ± 0.16; $P < 0.001$) (Fig EV1I and J). Thus, our observations collectively indicate that Nix is involved in Rheb-mediated mitophagy initiation through facilitating Rheb association with damaged mitochondria to promote mitochondrial targeting for autophagy.

We next sought to address whether enhanced mitochondrial recruitment of Rheb promotes mitophagosome formation in axons. Strikingly, following dissipation of $\Delta\psi_m$, axons expressing Rheb show a significant increase in the number of AVs and Mito-AVs/mitophagosomes (Ctrl: AVs: 7.41 ± 0.69; Mito-AVs: 3.51 ± 0.27; Rheb: AVs: 12.88 ± 0.45, $P < 0.001$; Mito-AVs: 6.77 ± 0.41, $P < 0.001$), accompanied by increased percentage of mitochondria within AVs (Ctrl: $21.99\% \pm 1.88\%$; Rheb: $42.76\% \pm 2.86\%$; $P < 0.001$; Fig 2A and B). Moreover, these mitophagosomes move exclusively in a retrograde direction, which is markedly enhanced in Rheb-expressed axons (Ctrl: $21.14\% \pm 3.52\%$; Rheb: $35.54\% \pm 2.90\%$; $P < 0.001$) (Fig 2A and C). This result supports our hypothesis that Rheb regulates mitophagosome biogenesis to remove damaged mitochondria from distal axons through retrograde transport.

To gain mechanistic insights into Rheb-mediated mitophagy, we performed a series of co-immunoprecipitation assays. Rheb forms a complex with LC3-II in cultured cortical neurons in the presence of CCCP (Fig EV2A). In transfected HeLa cells, the Rheb-LC3-II complex was detected upon treatment with CCCP, but not DMSO control. Moreover, Nix is associated with the Rheb-LC3-II complex (Fig EV2B and C). Our data suggest that, upon $\Delta\psi_m$ dissipation, Rheb promotes mitophagy by forming a complex with Nix and LC3-II. Given that Parkin is not present in HeLa cells, this result indicates that such a mechanism is independent of the Parkin pathway. We further conducted imaging studies to address whether Rheb and Nix, but not Parkin, are important for targeting damaged mitochondria for autophagy in axons. After CCCP treatment, the number of mitophagosomes and the percentage of mitochondria within AVs are remarkably reduced in axons expressing Rheb shRNA and Nix shRNA, but not Parkin shRNA and scrambled shRNA (Fig 2D and E). We and others previously demonstrated the knockdown efficiency of Parkin shRNA (Cai *et al*, 2012b; Rojansky *et al*, 2016). Together with our biochemical results, these findings collectively suggest that initiation of mitophagy in axons requires Rheb and Nix, but not Parkin.

We next determined whether the role of Rheb is specific to mitophagy, but not other forms of autophagy. We and others have shown that trehalose induces non-selective autophagy in neurons (Kruger *et al*, 2012; Feng *et al*, 2017). Consistently, trehalose treatment markedly increases the number of AVs within axons, compared to that of control axons treated with (DMSO: 0.25 ± 0.13; Tre: 9.82 ± 0.75, $P < 0.001$) (Fig EV2D and E). Importantly, Rheb RNAi has no detectable impact on trehalose-induced autophagy, as evidenced by the unaltered number of axonal AVs (9.74 ± 0.58; $P > 0.05$). There is no significant difference in the number of mitophagosomes within axons expressing scrambled shRNA and Rheb shRNA (Fig EV2F and G). In addition, Rheb is not associated with autophagosomes and mitochondria in axons upon autophagy induction by trehalose (Fig EV2H). Thus, these results suggest that Rheb plays a critical role in mitophagy, but not in non-selective autophagy.

We and others have demonstrated that Parkin-mediated mitophagy primarily occurs in the soma of neurons, where degradative lysosomes are highly enriched (Cai *et al*, 2010, 2012b; Devireddy *et al*, 2015; Xie *et al*, 2015; Ye *et al*, 2015; Maday & Holzbaur, 2016; Sung *et al*, 2016; Lin *et al*, 2017; Tammineni *et al*, 2017a; Cheng *et al*, 2018; Lee *et al*, 2019). We next examined whether Rheb is important for Parkin-mediated mitophagy. We previously showed that CCCP treatment robustly activates Parkin-mediated mitophagy, as reflected by increased Parkin translocation onto depolarized mitochondria (Cai *et al*, 2012a,b; Ye *et al*, 2015; Lin *et al*, 2017). Importantly, Rheb RNAi did not change the percentage of neurons showing Parkin association with mitochondria after $\Delta\psi_m$ dissipation (Fig EV2I and J), suggesting that Rheb is not involved in Parkin-dependent mitophagy in the soma. Thus, our data are consistent with previous work that Nix-mediated mitophagy is independent of the PINK1/Parkin pathway (Koentjoro *et al*, 2017).

To confirm our observations from imaging studies, we purified mitochondria-enriched factions from cultured cortical neurons treated with DMSO or CCCP. Excitingly, relative to control neurons incubated with DMSO, CCCP-treated neurons demonstrated a marked increase in Rheb association with depolarized mitochondria, coupled with elevated autophagy marker LC3-II levels in mitochondria-enriched factions (Rheb: 1.95 ± 0.35, $P < 0.01$; LC3-II: 2.56 ± 0.51, $P < 0.01$; Fig 2F and G). These data suggest that acute
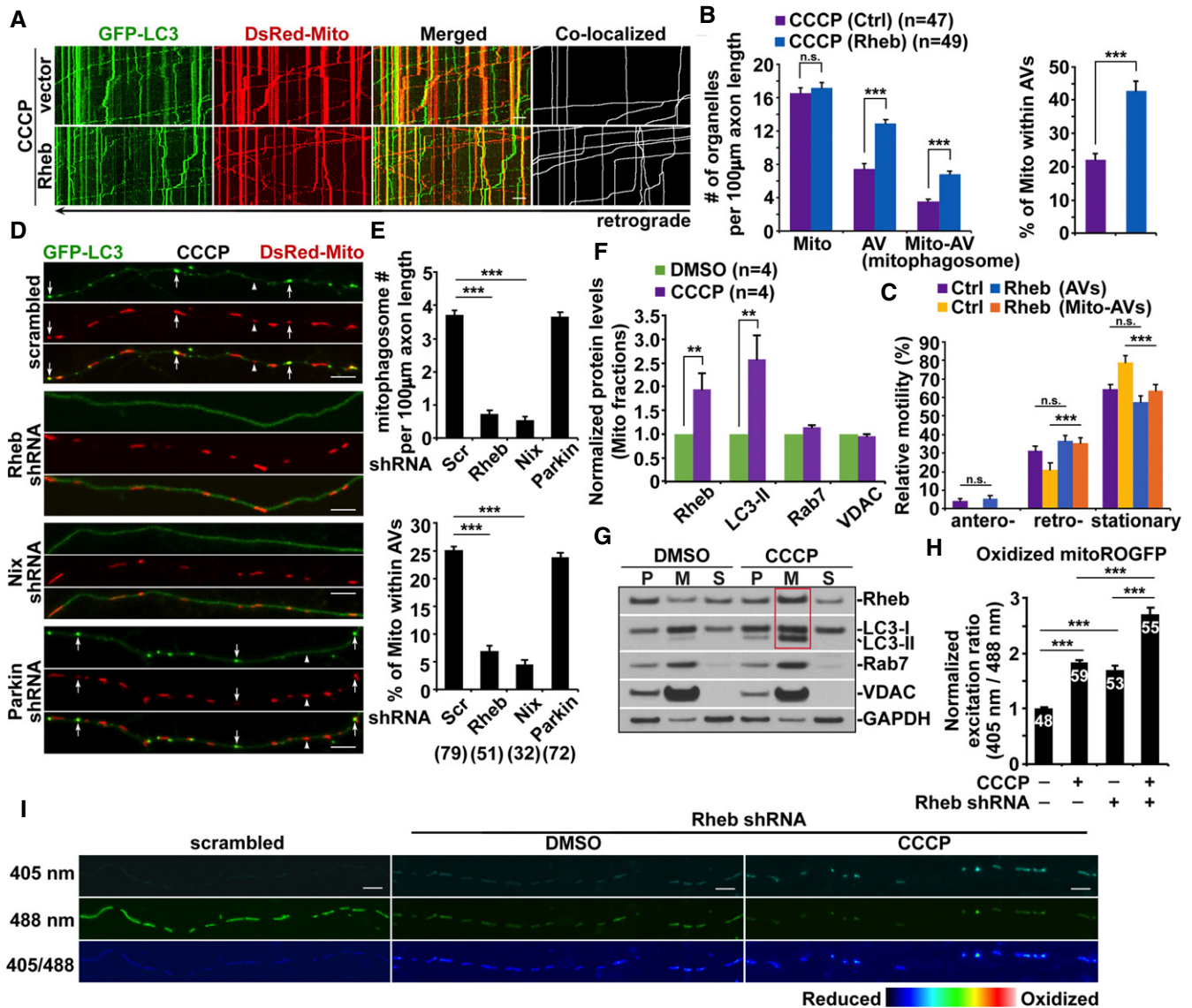
Figure 2. Rheb-mediated mitophagy in axons requires Nix but not Parkin.

A–C Representative dual-channel kymographs (A) and quantitative analysis (B, C) showing that overexpression of Rheb enhances mitophagy in CCCP-treated axons. The numbers of mitochondria (Mito), AVs, and Mito-AVs/mitophagosomes, the percentage of Mito within AVs, and the motilities of AVs and Mito-AVs along axons with and without elevated Rheb expression were quantified, respectively (B, C).

D, E Representative images (D) and quantitative analysis (E) showing that mitophagy in axons requires Rheb and Nix, but not Parkin. The number of mitophagosomes indicated by white arrows and the percentage of Mito within AVs in CCCP-treated axons expressing scrambled shRNA, Rheb shRNA, Nix shRNA, or Parkin shRNA were quantified, respectively (E).

F, G Quantitative analysis (F) and representative blots (G) showing increased mitochondrial association with Rheb and LC3-II in mature cortical neurons upon $\Delta\psi_m$ depolarization. Cortical neurons at 14 DIV were incubated with DMSO or 10 μM CCCP for 24 h and then subjected to fractionation into post-nuclear supernatant (P), mitochondria-enriched membrane fraction (M), and cytosolic supernatant (S). Equal amounts of protein (20 μg) were sequentially immunoblotted with antibodies against mitophagic/autophagic proteins Rheb, LC3, and Rab7, mitochondrial protein VDAC, and cytosolic protein GAPDH on the same membranes after stripping between each antibody application. The purity of mitochondrial fractions was confirmed by enrichment of VDAC and less abundance of GAPDH, compared to post-nuclear supernatant. Protein levels in mitochondrial fractions of CCCP-treated neurons were normalized to those in neurons incubated with DMSO. Data were quantified from four independent repeats.

H, I Quantitative analysis (H) and representative images (I) showing that Rheb RNAi augments axonal retention of oxidized mitochondria upon $\Delta\psi_m$ depolarization. The fluorescence of MitoROGFP was emitted at 510 nm and excited at 405 nm or 488 nm, respectively. Ratiometric images were generated from fluorescence excited by 405 nm light relative to that excited by 488 nm light. The ratio has been false-colored with the indicated heat map, with high intensity indicative of ROGFP fluorescence in a more oxidative level (I). Mean fluorescence intensity ratios evoked by the two excitation wavelengths at individual mitochondria in the CCCP-treated axons expressing scrambled shRNA or Rheb shRNA were quantified and normalized to those of control neurons transfected with scrambled shRNA (H).

Data information: Data were quantified from the total number of neurons (n) indicated in parentheses (B, E) or on the top of bars (H) from at least four experiments. Scale bars: 10 μm. Error bars represent SEM. Student's t-test: ***P < 0.001; **P < 0.01.

mitochondrial stress induces Rheb-associated mitophagy in neurons. We next examined whether Rheb-dependent mitophagy is critical for mitochondrial maintenance in axons. We knocked down Rheb using Rheb-small hairpin RNA (shRNA). Endogenous Rheb was remarkably reduced in cells expressing Rheb-shRNA, relative to those in scrambled shRNA expressed cells (Rheb-shRNA #1: 0.19 ± 0.04; $P < 0.001$; Rheb-shRNA #2: 0.16 ± 0.03; $P < 0.001$; Fig EV2K and L). Interestingly, Rheb RNAi efficiently impacts mitochondrial degradation, as reflected by increased levels of mitochondrial proteins TOM20 ($P < 0.05$) and SOD2 ($P < 0.001$). We assessed oxidatively stressed mitochondria in axons using Matrix-roGFP, RoGFP (reduction–oxidation-sensitive GFP) in mitochondrial matrix (Waypa et al, 2010; Xie et al, 2013). Oxidized mitochondria are increased in CCCP-treated axons, compared to those in control axons (1.83 ± 0.05, $P < 0.001$; Fig 2H and I). More importantly, under basal conditions, we observed significant retention of oxidatively stressed mitochondria within axons expressing Rheb-shRNA (1.71 ± 0.07, $P < 0.001$), which is augmented upon $\Delta\psi_m$ dissipation (2.71 ± 0.12, $P < 0.001$). Therefore, our findings support the notion that Rheb-mediated mitophagy facilitates mitophagic removal of stressed axonal mitochondria and thus plays a critical role in the maintenance of mitochondrial homeostasis in distal axons.

Presynaptic mitophagy stress in AD-related mutant hAPP Tg mouse brains

Given the involvement of Rheb in mitophagy initiation upon mitochondrial stress in the axons of WT neurons, we then assessed how Rheb-mediated mitophagy is regulated in response to chronic mitochondrial stress under pathophysiological conditions. We performed multiple lines of experiments and examined mitophagy in the axonal terminals of AD neurons. We first conducted immunostaining in AD-related mutant hAPP Tg mouse brains. In hippocampal mossy fibers enriched with axons and presynaptic terminals, LC3 immunostaining shows a diffuse pattern in WT mice, suggesting a non-lipidated LC3-I form in the cytoplasm (Fig 3A). In contrast, LC3 appears as vesicular structures in AD mouse brains. These structures represent lipidated LC3-II associated with autophagic vacuoles (AVs). Importantly, a majority of AVs also are positive for cytochrome c (Cyto c), a mitochondrial intermembrane space protein, suggesting that these AVs represent Mito-AVs/mitophagosomes— AVs containing engulfed mitochondria (WT: 3.67 ± 0.36; mutant hAPP: 26.08 ± 2.17, $P < 0.001$) (Fig 3A and B). Given the fact that Cyto c is released from damaged mitochondria into the cytoplasm, we examined mitophagic accumulation by using alternative antibodies against HSP60, a mitochondrial matrix protein, and p62, an autophagy marker. Consistently, we detected aberrant accumulation of mitophagosomes co-labeled by HSP60 and p62 in hippocampal mossy fiber regions of AD mouse brains (WT: 3.57 ± 0.30; mutant hAPP: 32.71 ± 3.41, $P < 0.001$) (Fig EV3A and B). Strikingly, mitophagosomes are concentrated within swollen/dystrophic presynaptic terminals surrounding amyloid plaques that are enriched with A11 antibody-marked soluble oligomeric Aβ (Figs 3C, and EV3C and D). Abnormal mitophagosome retention was also observed in the axons of cortical neurons cultured from mutant hAPP Tg mouse brains (Fig EV3E). Moreover, these mitophagosomes are positive for Rab7, indicating that they are mito-amphisomes in nature resulting from mitophagosome fusion with LEs

(Fig EV3F). Thus, our observations support the view that mitophagosomes aberrantly accumulate within AD synapses, which may contribute to synaptic damage.

Using transmission electron microscopy (TEM), we next assessed synaptic mitophagy at the ultrastructural level. Consistent with our light imaging data, we frequently detected mitophagosome-like structures at the hippocampal synapses in AD mouse brains (Fig 3E). Most of these are mito-amphisomes and are not readily observed in WT mouse brains. The percentage of presynaptic terminals containing mitophagosomes is markedly increased in AD mice, relative to that in WT littermate controls (WT: 12.11% ± 3.82%; mutant hAPP: 43.23% ± 7.91%, $P < 0.001$; Fig 3D). Meanwhile, synaptic mitochondrial density did not show a significant difference (WT: 45.82% ± 6.86%; mutant hAPP: 60.75% ± 7.52%, $P > 0.05$). To confirm these data, we purified synapse-enriched synaptosomes (Syn) using Percoll gradient centrifugations as previously described (DiGiovanni et al, 2012; Sepuri et al, 2017; Tammineni et al, 2017b; Ye et al, 2017). AD mice exhibit increased levels of LC3-II (6.24 ± 0.50, $P < 0.001$), p62/SQSTM1 (1.52 ± 0.09, $P < 0.001$), and Rab7 (1.57 ± 0.16, $P < 0.01$) along with Rheb (2.45 ± 0.38, $P < 0.01$), but not synaptophysin (SYP) and mitochondrial protein SOD2, compared to those of WT controls (Fig 3F and G). Soluble Aβ is enriched in the synaptosomal fractions from AD mouse brains. AD-associated synaptic mitophagy stress could be caused by enhanced mitophagy activation or impaired mitophagosome removal through retrograde transport. We next tested Rheb-dependent mitophagy in AD mouse brains. Relative to WT controls, Rheb is markedly elevated in mitochondria-enriched fractions (Mito) purified from AD mouse brains along with significantly increased levels of LC3-II, p62, and Rab7 (Rheb: 5.05 ± 1.18, $P < 0.01$; LC3-II: 30.65 ± 5.11, $P < 0.001$; p62: 3.65 ± 0.62, $P < 0.01$; Rab7: 3.93 ± 0.34, $P < 0.001$) (Fig 3H and I), suggesting robust activation of Rheb-related mitophagy in AD neurons. Therefore, our light imaging and TEM observations combined with biochemical results consistently indicate mitophagy stress at AD synapses.

Increased mitophagy initiation coupled with defective retrograde transport in AD axons

We next performed multiple lines of experiments to dissect the underlying mechanisms of synaptic mitophagy stress in AD neurons. We first determined whether mitophagy is efficiently initiated upon acute $\Delta\psi_m$ dissipation in cortical neurons derived from mutant hAPP Tg mouse brains. We observed increased Rheb targeting to mitochondria in AD axons, which is further enhanced following dissipating $\Delta\psi_m$ (WT: 14.53% ± 1.21%; mutant hAPP: 42.69% ± 2.13%; $P < 0.001$; with CCCP: 80.61% ± 1.41%; $P < 0.001$) (Fig 4A and B). Given that retrograde transport promotes efficient removal of newly formed mitophagosomes from distal axons, we next examined whether AD-linked synaptic mitophagy stress is the result of impaired retrograde transport. Indeed, retrograde movement of mitophagosomes is markedly reduced (2.40% ± 0.96%), coupled with increased mitophagic accumulation within AD axons (number: 5.50 ± 0.48; percentage of Mito within AVs: 34.82% ± 2.97%; Fig 4C–E). Moreover, CCCP treatment exacerbates mitophagic accumulation as a result of defective retrograde transport (retrograde: 2.89% ± 0.70%; number: 10.00 ± 0.44; percentage: 50.73% ± 2.13%), suggesting that mitophagy stress at
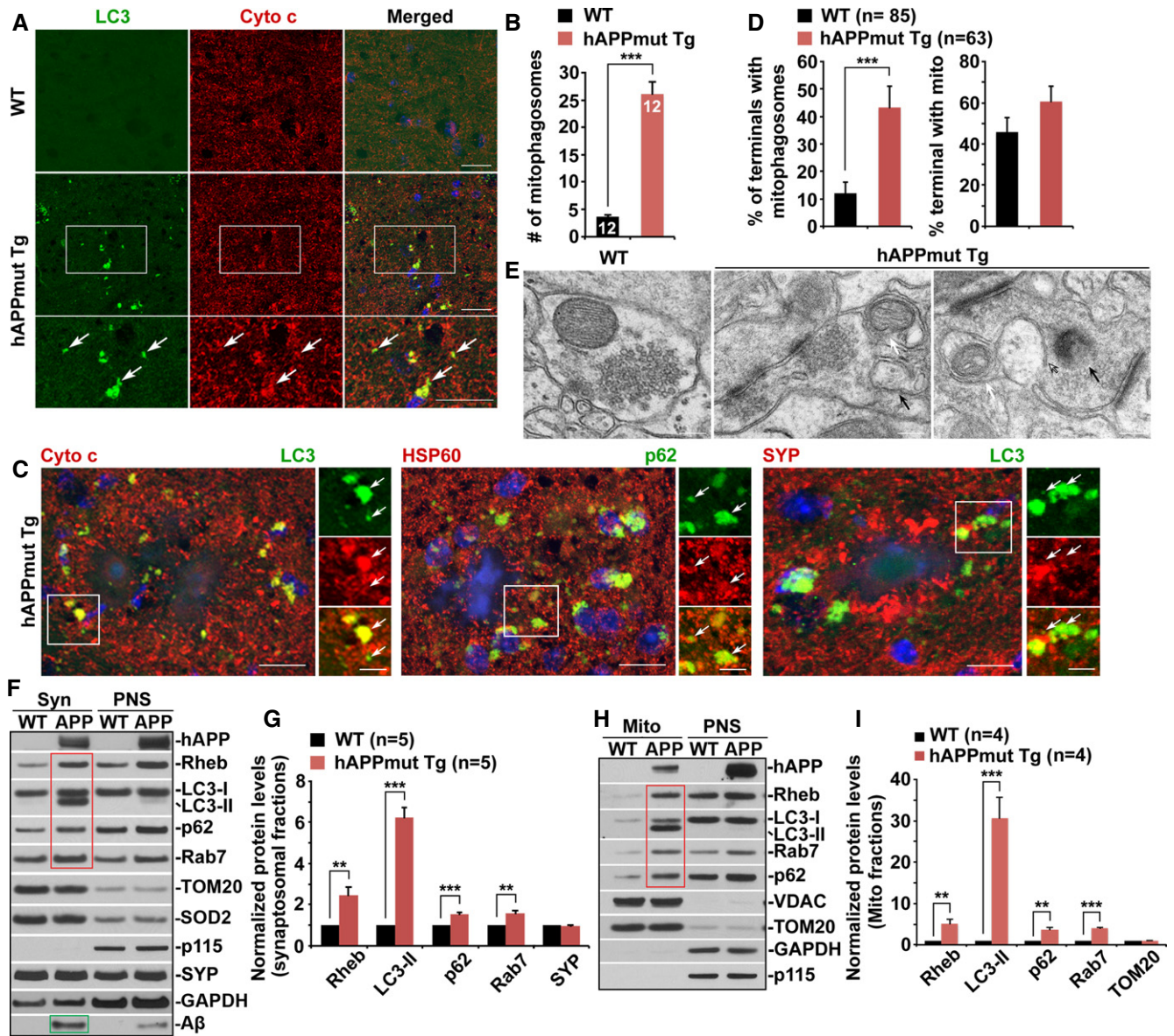
Figure 3. Presynaptic mitophagy stress in AD-related mutant hAPP Tg mouse brains.

A, B Aberrant accumulation of mitophagosomes co-labeled by antibodies against LC3 and cytochrome *c* (Cyto *c*) in the hippocampal mossy fibers of mutant hAPP Tg mouse brains. Note that mitophagosomes indicated by white arrows are not readily observed in WT mouse brains (A). The average number of mitophagosomes per section (320 μm × 320 μm) was quantified from the total number of brain slice sections (*n*) indicated on the top of the bars (B).

C Clustering of mitophagosomes (white arrows) co-labeled by antibodies against LC3 and Cyto *c* or p62 and HSP60 within swollen/dystrophic presynaptic terminals indicated by synaptophysin (SYP) surrounding amyloid plaques in AD mouse brains.

D, E Quantitative analysis (D) and representative TEM images (E) showing presynaptic retention of mitophagosome-like structures in the hippocampal regions of mutant hAPP mouse brains. White arrow-labeled mitophagosomes are not readily detected in WT mouse brains. Black arrows marked amphisomes or degradative autophagic vacuoles (AVd). Data were quantified from the total number of the imaging fields (*n*) indicated in parentheses (D).

F, G Mitophagic accumulation at Aβ-enriched synapses in AD mouse brains. Note that the levels of mitophagic/autophagic proteins (red box) along with Aβ (green box) are increased in synaptic fractions isolated from AD mouse brains. Equal amounts (10 μg) of synaptosomal preparations (Syn) and post-nuclear supernatants (PNS) from WT and mutant hAPP mouse brains were sequentially immunoblotted with antibodies against hAPP/Aβ, Rheb, LC3, p62, and Rab7, as well as mitochondrial proteins TOM20 and SOD2 on the same membrane after stripping between each antibody application. The purity of synaptosomal fractions was confirmed by relative enrichment of SYP and less abundance of p115 and GAPDH (F). Relative protein levels in the synaptosomal preparations from mutant hAPP mice were compared to those in WT littermate controls. Data were quantified from five repeats (G).

H, I Representative blots (H) and quantitative analysis (I) showing increased levels of Rheb along with LC3-II, p62, and Rab7 (red box) in mitochondrial (Mito) fractions purified from AD mouse brains. The purity of Mito fractions was confirmed by enrichment of mitochondrial proteins VDAC and TOM20 and by the absence of GAPDH and p115, relative to PNS fractions. Data were quantified from four repeats (I).

Data information: Scale bars: 25 μm (A, C); 10 μm (C at high magnification); 200 nm (E). Error bars represent SEM. Student's *t*-test: ***$P < 0.001$; **$P < 0.01$.

AD synapses is likely attributed to defects in retrograde transport and thus impaired removal of mitophagosomes from axonal terminals.

Consistently, after CCCP treatment, AD neurons exhibit additional increase in mitochondrial recruitment of Rheb, accompanied with elevated mitochondrial association with LC3-II and Rab7 (Rheb: 4.31 ± 1.18, $P < 0.05$; LC3-II: 3.37 ± 0.29, $P < 0.001$; Rab7: 1.44 ± 0.16, $P < 0.05$; Fig 4F and G), indicating augmentation of Rheb-dependent mitophagy. Combined with a marked increase of Rheb in synaptosomal fractions and synaptic mitophagic accumulation in AD mouse brains (Fig 3), these data consistently indicate that Rheb-mediated mitophagy is markedly activated at AD synapses. More importantly, relative to WT controls, we found accumulation of oxidatively stressed mitochondria in AD axons, which is augmented after CCCP treatment (1.86 ± 0.03, CCCP: 2.98 ± 0.05; $P < 0.001$) (Fig 4H and I). These data indicate that mitophagy failure in AD axons impairs removal of damaged mitochondria, thereby exacerbating mitochondrial defects.

Mitophagy is a lysosome-dependent pathway, and alterations in the lysosomal system have been implicated in AD (Nixon, 2013; Menzies et al, 2015). Thus, we next determined the lysosomal impact on mitophagy in the axons of WT and AD neurons. To examine the distribution of mitochondria within acidic lysosomal organelles, we utilized mt-Keima, a ratiometric pH-sensitive fluorescent probe, which targets to the mitochondrial matrix (Katayama et al, 2011). A short wavelength (440 nm) is predominant for excitation in a neutral environment (neutral mito), whereas a long wavelength (586 nm) is predominant in an acidic environment (acidic mito). We found that acidic mitochondria are exclusively located in the soma of neurons (Fig EV4A and B). The number of acidic mitochondria was elevated in the presence of CCCP, and additional increase was shown in the soma of neurons treated with CCCP and lysosomal inhibitors (LIs) (DMSO: 7.83 ± 0.55; CCCP: 21.16 ± 0.73; CCCP+LIs: 35.23 ± 1.41; $P < 0.001$). We failed to detect acidic mitochondria in axons under these conditions (Fig EV4A). Our observations are consistent with previous studies showing that acidic mitochondria, visualized by mt-Keima, are mostly detected in the soma, but not in axons (Bingol et al, 2014; Puri et al, 2019). Furthermore, we confirmed a strong co-localization of these acidic mitochondria with somatic lysosomes marked by LAMP1, suggesting that they are mitolysosomes in nature. Consistently, treatments with CCCP or CCCP and LIs lead to a significant increase in the number of mitolysosomes (Fig EV4C and D). These findings collectively support the notion that mitophagic clearance mainly occurs in the soma, where mature lysosomes are mainly located.

We next examined whether mitolysosomes accumulate in AD neurons. Compared to WT neurons derived from littermate controls, mitolysosomes are retained in the soma of mutant hAPP neurons. Lysosomal defects have been indicated in APP/PS1 Tg and PS1KO mice and cells (Lee et al, 2010; Neely Kayala et al, 2012; Zhang et al, 2012; Hung & Livesey, 2018). To further address the impact of lysosomal deficiency on mitophagy in AD neurons, we transfected mutant hAPP neurons with familial AD (FAD)-associated mutations PS1L286E (Kulic et al, 2000). Mitolysosomal retention is enhanced in mutant hAPP neurons co-expressing mutant PS1L286E (WT: 7.83 ± 0.54; hAPPmut: 28.98 ± 0.67; hAPPmut with PS1mut: 43.27 ± 0.72; $P < 0.001$;

Fig EV4E and F). $\Delta\psi_m$ dissipation further augments such retention in these AD neurons (hAPPmut: 48.36 ± 1.21; hAPPmut with PS1mut: 58.08 ± 1.19; $P < 0.001$). Importantly, while these results are consistent with increased retention of acidic mitochondria in the soma (Fig EV4G and H), acidic mitochondria cannot be detected within the axons of these AD neurons with or without mutant PS1 expression or in the presence or absence of CCCP (Fig EV4I). Therefore, these results suggest that lysosomal deficiency has no direct impact on mitophagy stress in the axons of AD neurons.

Deficiency in Snapin-mediated retrograde transport recapitulates presynaptic mitophagy stress and leads to synaptic defects in mouse brains

Our previous studies revealed that dynein–Snapin, the motor–adaptor complex, mediates retrograde transport of AVs to reduce autophagic accumulation in distal axons (Cheng et al, 2015a,b; Tammineni & Cai, 2017; Tammineni et al, 2017b). We examined whether dynein–Snapin-mediated retrograde transport is involved in the removal of mitophagosomes from axonal terminals. We found increased mitophagosome clusters in the hippocampal mossy fibers of snapin-deficient mice (WT: 3.64 ± 0.41; snapin cKO: 28.55 ± 2.36, $P < 0.001$) (Fig 5A and B). In purified Syn and Mito fractions from conditional snapin-KO mouse brains, we detected synaptic retention of Rheb-associated mitophagosomes, as reflected by increased levels of Rheb along with LC3-II, p62, and Rab7 (Syn: Rheb: 2.68 ± 0.49, $P < 0.01$; LC3-II: 10.64 ± 2.15, $P < 0.001$; p62: 1.73 ± 0.28, $P < 0.05$; Rab7: 1.62 ± 0.19, $P < 0.01$; Mito: Rheb: 2.68 ± 0.40, $P < 0.01$; LC3-II: 17.00 ± 3.39, $P < 0.001$; p62: 3.20 ± 0.86, $P < 0.05$; Rab7: 1.53 ± 0.13, $P < 0.05$) (Fig 5C–F). These results indicate that defects in Snapin-mediated retrograde transport induce synaptic mitophagic accumulation, mimicking mitophagy stress at AD synapses. Consistent with our light imaging study from AD mouse brains, the result from TEM analysis showed marked mitophagosome accumulation at hippocampal synapses in snapin-mutant mice. These mitophagosomes represent mito-amphisome-like structures (WT: $14.58\% \pm 4.76\%$; snapin cKO: $44.13\% \pm 8.80\%$, $P < 0.001$; Fig 5G and H). Furthermore, the density of presynaptic terminals labeled by synaptophysin (SYP) is significantly reduced in the hippocampal mossy fiber regions of snapin cKO mice (0.84 ± 0.02, $P < 0.001$; Fig 5I and J). Thus, our data suggest that Snapin-mediated retrograde transport promotes mitophagic removal of defective mitochondria from distal axons, and such a mechanism is critical for synaptic maintenance.

Snapin-enhanced retrograde transport reduces mitophagic accumulation and attenuates mitochondrial defects in mutant hAPP Tg axons

Given that defective retrograde transport impairs synaptic removal of mitophagosomes, we next determined whether Snapin-enhanced retrograde transport reduces mitophagy stress in AD axons. Excitingly, upon dissipating $\Delta\psi_m$, AD neurons expressing Snapin display a significant increase in retrograde transport of mitophagosomes (Snapin: $22.38\% \pm 1.53\%$, $P < 0.001$), accompanied with decreases in mitophagosomal accumulation (Snapin: 5.25 ± 0.30, $P < 0.001$) and percentage of mitochondria within AVs (Snapin:
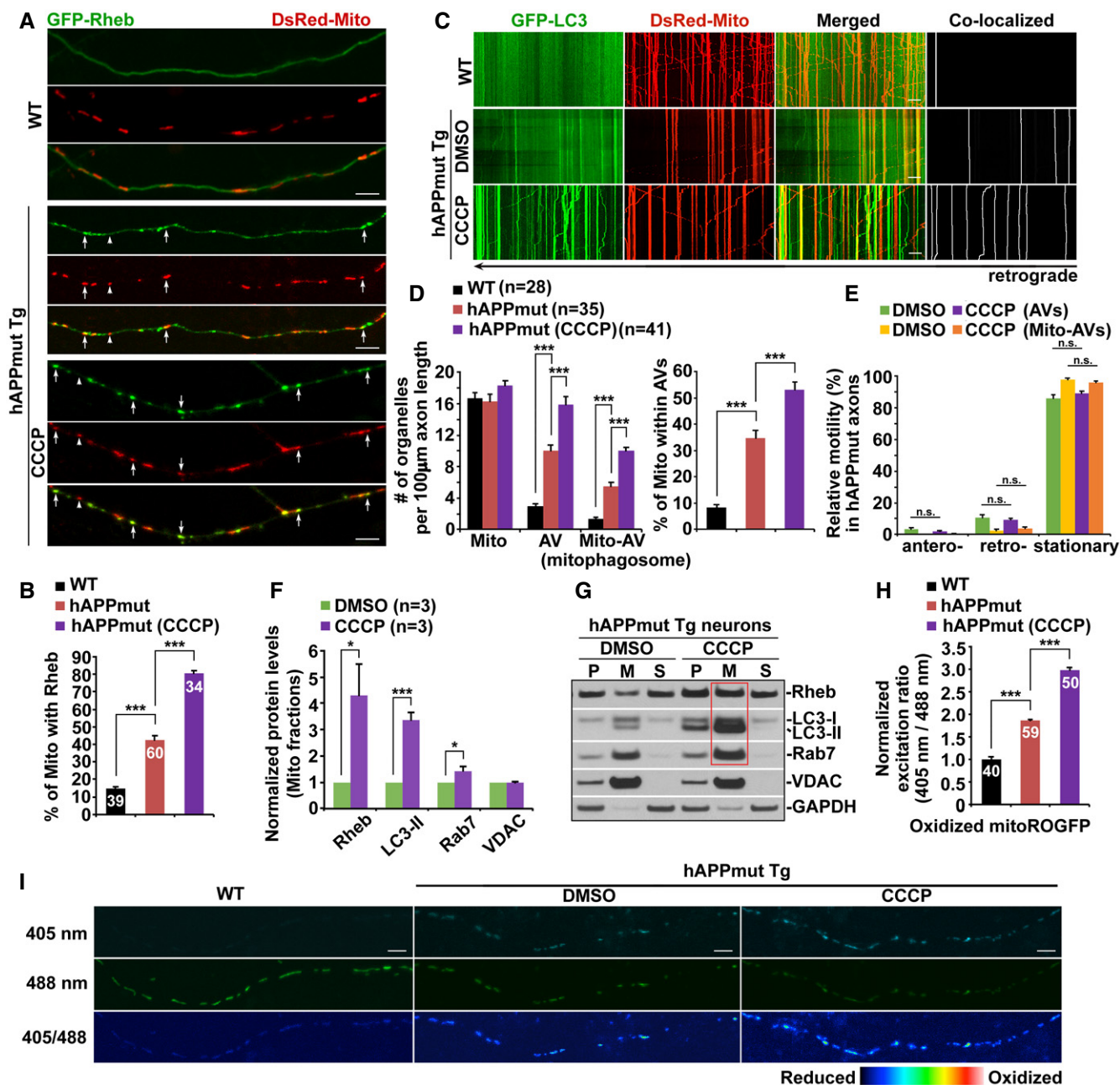
Figure 4. Increased mitophagy initiation coupled with defective retrograde transport in AD axons.

A, B   Representative images (A) and quantitative analysis (B) showing increased mitochondrial association with Rheb in AD axons, relative to that of WT littermate controls. Note that CCCP treatment enhances Rheb localization to mitochondria. The percentages of white arrow-marked mitochondria that were targeted by Rheb in WT and mutant hAPP axons in the absence and presence of CCCP were quantified, respectively (B).

C–E   Representative dual-channel kymographs (C) and quantitative analysis (D, E) showing defective retrograde transport and mitophagic accumulation within AD axons. Relative motility of AVs and Mito-AVs/mitophagosomes, the numbers of Mito, AVs, and Mito-AVs, and the percentage of mitochondria within AVs in WT or mutant hAPP axons with and without CCCP were quantified, respectively (D, E).

F, G   Quantitative analysis (F) and representative blots (G) showing that $\Delta\psi_m$ depolarization augments mitophagy activation in cortical neurons cultured from AD mouse brains. Note increased localization of Rheb along with LC3-II and Rab7 to mitochondria in mutant hAPP Tg neurons after CCCP treatment (red box). Data were quantified from three independent repeats. P: post-nuclear supernatants; M: mitochondria-enriched membrane fractions; S: cytosolic supernatants.

H, I   Quantitative analysis (H) and representative images (I) showing abnormal accumulation of oxidatively damaged mitochondria in AD axons, which is exacerbated after dissipating $\Delta\psi_m$. Mean fluorescence intensity ratios evoked by the two excitation wavelengths (405 and 488 nm) at individual mitochondria in mutant hAPP axons with and without CCCP treatment were quantified and normalized to those of WT controls (H).

Data information: Data were quantified from the total number of neurons (*n*) indicated on the top of the bars (B, H) or in parentheses (D) from more than four independent experiments. Scale bars: 10 μm. Error bars represent SEM. Student's *t*-test: ***$P < 0.001$; *$P < 0.05$.

26.46% ± 1.07%, P < 0.001) (Fig 6A–C). Importantly, such a rescue effect cannot be detected in AD axons expressing Snapin-L99K, a dynein motor binding-deficient mutant of Snapin, suggesting that reduced mitophagy stress in AD axons is specifically attributed to Snapin-enhanced retrograde transport. Moreover, increased mitophagic removal of stressed mitochondria in AD axons with overexpression of Snapin, but not Snapin-L99K, ameliorates axonal mitochondrial defect, as reflected by a marked reduction of oxidatively damaged mitochondria (0.72 ± 0.02, P < 0.001) (Figs 6D and EV5A). Moreover, the expression levels of Snapin and Snapin-L99K are similar in transfected cells (Fig EV5B).

Overexpression of Snapin ameliorates mitophagy stress and mitigates synapse loss in mutant hAPP Tg mouse brains

We hypothesized that Snapin-enhanced mitophagy and attenuation of mitochondrial deficit mitigate AD-associated synaptic damage. To test this hypothesis, we infected mutant hAPP Tg mouse brains at the age of 2–3 months with AAV-mCherry or AAV-mCherry-IRES-Snapin by bilateral injection into the hippocampus, an established in vivo delivery procedure (Nagahara et al, 2009, 2013; Polito et al, 2014; Xiao et al, 2015; Xie et al, 2015; Ye et al, 2017). The majority of neurons in the hippocampal CA3 and dentate gyrus and their processes in hippocampal mossy fibers were infected (Fig 7A).
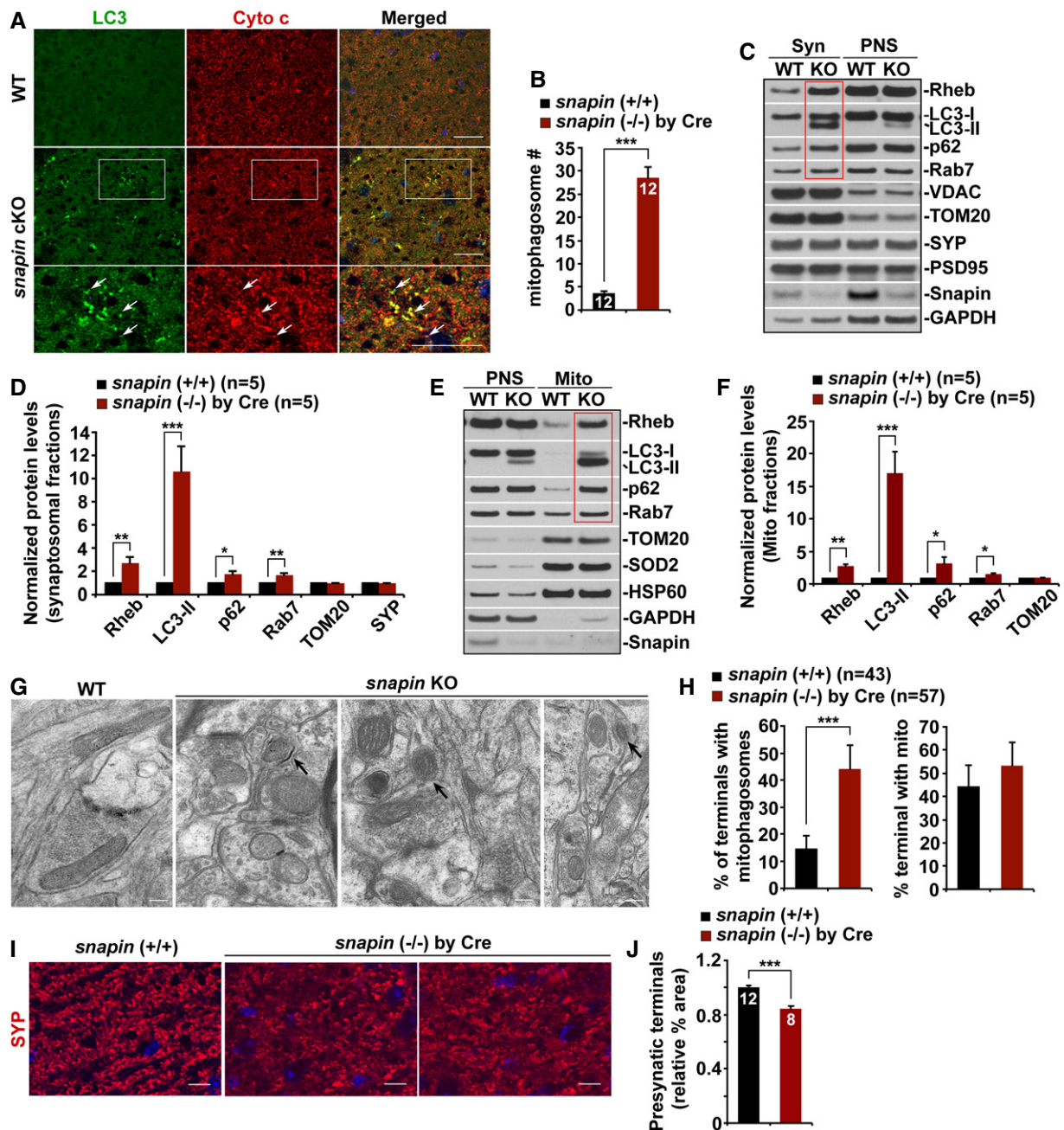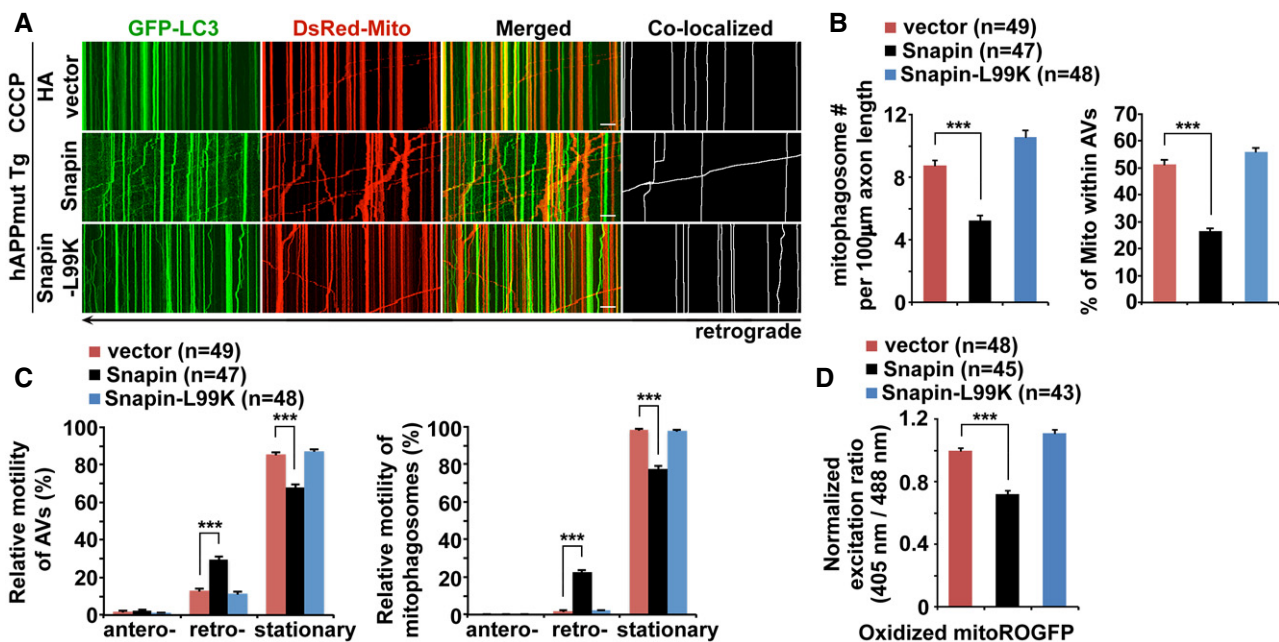

Figure 5.

Figure 5. Deficiency in Snapin-mediated retrograde transport recapitulates presynaptic mitophagy stress and leads to synaptic defects in mouse brains.

A, B Representative images (A) and quantitative analysis (B) showing aberrant accumulation of mitophagosomes labeled by LC3 and Cyto *c* antibodies in the hippocampal mossy fibers of *snapin* cKO mouse brains. Note that white arrow-labeled mitophagosomes are not readily observed in WT mouse brains. The average number of mitophagosomes per section (320 μm × 320 μm) was quantified.

C, D Representative blots (C) and quantitative analysis (D) showing aberrant mitophagic retention at synaptic terminals in *snapin*-mutant mouse brains. The levels of Rheb along with LC3-II, p62, and Rab7 are significantly elevated in the synaptosomal fractions (Syn) purified from *snapin*-deficient mouse brains, relative to those of WT littermate controls (red box). Equal amounts (10 μg) of Syn and post-nuclear supernatants (PNS) from WT and *snapin*-mutant mouse brains were sequentially immunoblotted with antibodies against Snapin, mitophagic/autophagic proteins, and mitochondrial proteins VDAC and TOM20 on the same membrane after stripping between each antibody application. The purity of synaptosomal fractions was confirmed by relative enrichment of synaptophysin (SYP) and PSD95 and less abundance of GAPDH. Data were quantified from five independent repeats.

E, F Representative blots (E) and quantitative analysis (F) showing mitophagic accumulation in the brains of *snapin* conditional KO (cKO) mice by crossing with Thy1-cre Tg mice. Note increased levels of Rheb along with LC3-II, p62, and Rab7 in mitochondrial (Mito) fractions isolated from *snapin*-deficient mouse brains (red box), relative to those of WT littermate controls. Data were quantified from five independent repeats. PNS: post-nuclear supernatants.

G, H Representative TEM images (G) and quantitative analysis (H) showing abnormal presynaptic retention of mitophagosome-like structures in the hippocampal regions of *snapin*-deficient mouse brains. Mitophagosomes, indicated by black arrows, are not readily detected in WT mouse brains. Data were quantified from the total number of the imaging fields (*n*) indicated in parentheses (H).

I, J Representative images (I) and quantitative analysis (J) showing that deletion of *snapin* in mouse brains induces synaptic damage. Note that the density of presynaptic terminals in the hippocampal mossy fibers revealed by SYP immunostaining is significantly reduced in *snapin*-mutant mice crossed with CamKII-cre Tg mice at the age of 8 months, relative to that of WT littermate controls.

Data information: Data were quantified from the total number of brain slice sections (*n*) indicated on the top of the bars (B, J). Scale bars: 25 μm (A); 10 μm (I); 200 nm (G). Error bars represent SEM. Student's *t*-test: ***$P < 0.001$; **$P < 0.01$; *$P < 0.05$.

Figure 6. Snapin-enhanced retrograde transport reduces mitophagic accumulation and attenuates mitochondrial defects in mutant hAPP Tg axons.

A–C Representative dual-channel kymographs (A) and quantitative analysis (B, C) showing that overexpression of Snapin, but not Snapin-L99K, a Snapin mutant deficient in dynein motor binding, enhances retrograde transport of mitophagosomes and reduces mitophagic accumulation within AD axons incubated with CCCP.

D Mean fluorescence intensity ratios evoked by 405 and 488 nm excitation wavelengths at individual mitochondria in mutant hAPP axons expressing Snapin or Snapin-L99K were quantified and normalized to those of mutant hAPP controls. Note that oxidatively stressed mitochondria are reduced within AD axons expressing Snapin after CCCP treatment.

Data information: Data were quantified from the total number of neurons (*n*) indicated in parentheses (B, C, D) from more than four independent experiments. Scale bars: 10 μm. Error bars represent SEM. Student's *t*-test: ***$P < 0.001$.

Snapin expression was verified by Western blot analysis, which revealed increased Snapin levels in the hippocampus of Snapin-injected AD mice at the age of 7 months (1.85 ± 0.18, $P < 0.01$) (Fig EV5C and D). Interestingly, AD mouse brains transduced with AAV-Snapin exhibit reduced mitophagosome accumulation in the hippocampal mossy fiber areas, compared to that in control AD mice expressing AAV-mCherry (Ctrl: 18.69 ± 1.30; Snapin: 7.07 ± 0.59; $P < 0.001$; Fig 7B and C). Immunostaining using antibodies against HSP60 and p62 showed a similar result (Ctrl: 17.02 ± 0.91; Snapin: 7.51 ± 0.65; $P < 0.001$; Fig EV5E and F). Our
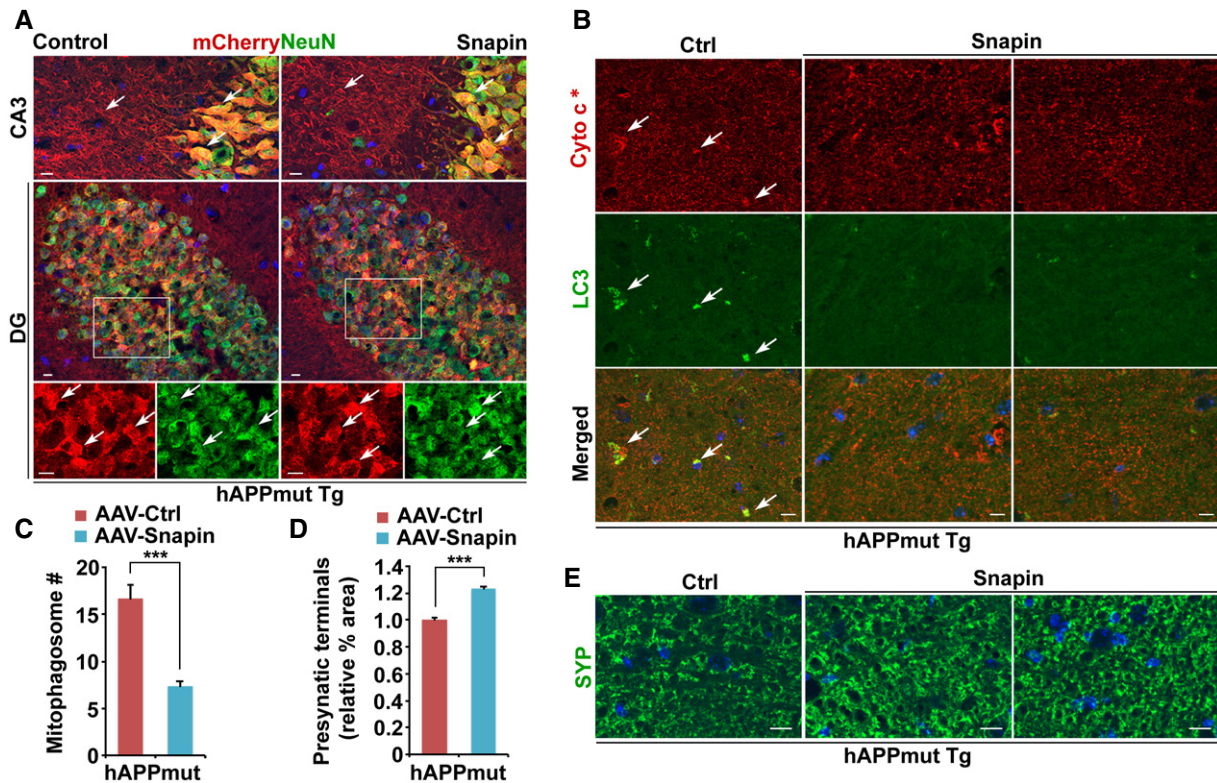
Figure 7. Overexpression of Snapin ameliorates mitophagy stress and mitigates synapse loss in mutant hAPP Tg mouse brains.

A   Representative images showing gene delivery into the hippocampus of AD mice injected with AAV-mCherry or AAV-mCherry-Snapin. mCherry fluorescence indicated by white arrows is present in the soma and processes of transduced neurons in the hippocampal CA3 and dentate gyrus (DG) of mutant hAPP mouse brains. NeuN, a neuronal nuclear marker, indicates neurons.

B, C   Attenuation of mitophagic accumulation in the hippocampal mossy fibers of AD mice transduced with AAV-mCherry-Snapin. Note a marked reduction of mitophagosomes (white arrows) in mutant hAPP Tg mouse brains with elevated Snapin expression (C). Cyto *c**: color is converted to red for better contrast (B).

D, E   Quantitative analysis (D) and representative images (E) showing increased density of presynaptic terminals in the hippocampal mossy fibers of AD mice infected with AAV-mCherry-Snapin. Blue indicates the signal of DAPI staining. The percentage area of synaptophysin (SYP)-labeled presynaptic terminals was quantified and normalized to that of control AD mice injected with AAV-mCherry (D).

Data information: Data were quantified from a total number of 40–44 imaging slice sections of three pairs of mutant hAPP Tg mice with AAV injection. Scale bars: 10 μm. Error bars represent SEM. Student's *t*-test: ****P* < 0.001.

data suggest that Snapin-enhanced retrograde transport ameliorates AD-linked distal mitophagy stress. Synapse loss at early disease stages in this mouse line has been well established from previous studies (Mucke *et al*, 2000; Nagahara *et al*, 2009, 2013; Ye *et al*, 2017). Strikingly, AAV-Snapin transduction leads to increased density of presynaptic terminals in the hippocampal mossy fibers of AD mice, compared to that of control mice (1.23 ± 0.01, *P* < 0.001; Fig 7D and E). Thus, these *in vitro* and *in vivo* beneficial effects consistently support our hypothesis that enhanced mitophagic removal of defective mitochondria through retrograde transport attenuates synaptic mitochondrial deficits and thus mitigates synaptic defects in AD brains.

Discussion

Synaptic mitochondria play a pivotal role in sustaining synaptic activities, but are more vulnerable to cumulative changes induced by deleterious factors such as Aβ. Synaptic stress is an early

pathological feature of AD, and mitochondrial deficit has been proposed as a key player in synaptic damage in AD (Reddy & Beal, 2008; Reddy *et al*, 2010; Reddy, 2011; Du *et al*, 2012; Cai & Tammineni, 2017; Tonnies & Trushina, 2017). However, critical understanding of the mitochondrial quality control mechanism at nerve terminals remains very limited. Our study provides the first indication that Rheb and Snapin serve as key players in mitophagy-mediated regulation of mitochondrial integrity at synapses, and mitophagy failure is involved in synaptic mitochondrial deficits and synaptic deterioration associated with AD.

Recent studies have shown mitophagic abnormalities in AD, particularly in the PINK1/Parkin pathway (Ye *et al*, 2015; Du *et al*, 2017; Manczak *et al*, 2018; Reddy *et al*, 2018; Cummins *et al*, 2019; Fang *et al*, 2019). For instance, our studies have revealed that Parkin-mediated mitophagy is induced at early disease stages in the brains of AD patients and mouse models, but cytosolic depletion of Parkin over disease progression leads to defective mitophagy and aberrant accumulation of damaged mitochondria in AD neurons (Ye *et al*, 2015). Defects in Parkin-mediated mitophagy were also

reported in neuroblastoma cells and the *Caenorhabditis elegans* nervous system under tauopathy conditions (Cummins *et al*, 2019). While AD brains display reduced levels of PINK1 and TERT (Manczak *et al*, 2018; Reddy *et al*, 2018), PINK1 overexpression was shown to ameliorate cognitive dysfunction in AD mice by promoting the clearance of damaged mitochondria (Du *et al*, 2017). A recent study further demonstrated that the basal level of mitophagy is also reduced in AD brains (Fang *et al*, 2019). Importantly, enhancement of PINK-1-dependent mitophagy abolishes AD pathology and reverses memory deficits in AD models. These studies collectively suggest a critical role of PINK1/Parkin-mediated mitophagy in AD pathophysiology. Damaged mitochondria recruit Parkin to initiate mitophagy for subsequent degradation within lysosomes (Youle & Narendra, 2011; Pickrell & Youle, 2015; Pickles *et al*, 2018). We and others have shown that Parkin-mediated mitophagy primarily occurs in the neuronal soma, where degradative lysosomes are highly enriched (Cai *et al*, 2010, 2012b; Devireddy *et al*, 2015; Xie *et al*, 2015; Ye *et al*, 2015; Maday & Holzbaur, 2016; Sung *et al*, 2016; Lin *et al*, 2017; Tammineni *et al*, 2017a; Cheng *et al*, 2018; Lee *et al*, 2019). This raises the possibility that alternative mechanism(s) must function to efficiently remove constantly damaged mitochondria from axonal terminals to maintain mitochondrial homeostasis under disease-associated chronic stress conditions. In the current study, we uncover a new mechanism of mitochondrial quality control in axons which involves Rheb-dependent mitophagy initiation and dynein–Snapin-mediated retrograde transport. Such a mechanism is essential for the maintenance of synaptic mitochondrial integrity. Moreover, we hypothesize that increased mitophagy initiation along with defects in retrograde transport leads to mitophagic accumulation and mitochondrial stress, thereby exacerbating synaptic deficits in AD neurons. Excitingly, Snapin-enhanced retrograde transport alleviates mitochondrial defects and mitigates synapse loss in AD mouse brains. Thus, in line with previous understandings of PINK1/Parkin-mediated mitophagy in the soma, our current work not only advances our understanding of the mechanism underlying mitochondrial maintenance through mitophagy at synaptic terminals, but also provides new insights into the critical role of mitophagy dysfunction in AD-linked synaptic mitochondrial deficits and synaptic damage.

Rheb is well established as an activator of mammalian target of rapamycin (mTOR), a kinase with diverse cellular function (Manning & Cantley, 2003; Groenewoud & Zwartkruis, 2013). A growing body of evidence suggests that Rheb is involved in multiple cellular processes including protein synthesis (Tyagi *et al*, 2015; Nnah *et al*, 2019). Rheb was also reported to regulate BACE1 levels and thus APP processing (Shahani *et al*, 2014, 2017). Rheb was shown to protect against neurodegeneration and mediate axonal regrowth in dopaminergic neurons, attributable to activation of the neurotrophic signaling pathway (Kim *et al*, 2012). The role of Rheb in mitophagy has recently been described in HeLa, muscle, and macrophage cells, and is independent of that in Rheb-mediated mTOR activation (Melser *et al*, 2013; Yang *et al*, 2014; Kang *et al*, 2016). In particular, in response to increased mitochondrial energetics, Rheb initiates mitophagy through association with mitochondrial outer membrane, and then its physical interaction with LC3-II on mitochondria mediates autophagic recruitment (Melser *et al*, 2013). However, the outstanding questions remain: Whether mitochondrial damage, but not increased mitochondrial respiration, activates Rheb-associated

mitophagy, and whether this mechanism is involved in mitochondrial quality control in healthy and diseased neurons. Addressing these questions will also advance our understanding of the mechanisms underlying AD-linked mitochondrial pathology and synaptic deterioration. The current study reveals that Rheb senses $\Delta\psi_m$ depolarization to initiate mitophagy in distal axons under both physiological and pathophysiological conditions. Rheb-associated mitophagy initiation within axons requires Nix, but is independent of the Parkin-mediated pathway in the soma of neurons (Figs 2, and EV1 and EV2). Moreover, Rheb is important for mitophagy, but not other forms of autophagy (Fig EV2E–H). Rheb loss of function impairs mitochondrial maintenance within axons, as reflected by abnormal retention of oxidatively stressed mitochondria (Fig 2H and I). Furthermore, Rheb effectively responds to AD-linked chronic mitochondrial stress conditions by mediating the targeting of stressed mitochondria for autophagy at AD synapses (Fig 4). Therefore, we reveal, for the first time, that Rheb-mediated mitophagy plays a critical role in the quality control of mitochondria within the axons of healthy and diseased neurons.

Our previous studies reported a critical role of Snapin, a dynein motor adaptor, in the regulation of LE retrograde axonal transport and autophagy function in neurons (Cai *et al*, 2010; Cai & Sheng, 2011). Snapin interacts with the dynein intermediate chain (DIC), enabling dynein motor recruitment to LEs for long-distance retrograde transport. It has been established that autophagosomes are robustly generated in distal axons and move in a retrograde direction for lysosomal clearance in the soma (Maday *et al*, 2012; Cheng *et al*, 2015a,b; Maday & Holzbaur, 2016). Our work further shows that nascent autophagosomes recruit dynein–Snapin transport machinery to gain retrograde transport motility through fusion with LEs to form amphisomes. Such a mechanism facilitates autophagic clearance within lysosomes in the soma (Cheng *et al*, 2015a, b). In the current study, we provide new evidence showing that Rheb-dependent mitophagy initiation coordinates with dynein–Snapin-mediated retrograde transport to promote removal of mitophagosomes and thus reduces mitochondrial stress in distal axons, a process critical for synaptic mitochondrial maintenance. Interestingly, our results suggest that newly generated mitophagosomes fuse rapidly with LEs to form amphi-mitophagosomes, allowing mitophagosomes to load dynein–Snapin transport machinery and enabling their retrograde transport motility (Figs 2 and EV1). Moreover, we propose that defects in dynein–Snapin-mediated retrograde transport exacerbate mitophagic accumulation at AD synapses. We have previously demonstrated that soluble oligomeric Aβ_{1-42} disrupts dynein motor-Snapin coupling and thus impairs dynein motor recruitment to AVs, leading to defective AV retrograde transport in AD axons (Tammineni & Cai, 2017; Tammineni *et al*, 2017b; Winckler *et al*, 2018). Mitophagosomes are concentrated in AD synapses enriched with oligomeric Aβ (Figs 3F and EV3C). Therefore, this supports the view that impaired retrograde transport of mitophagosomes is likely attributed to soluble oligomeric Aβ-mediated disruption of dynein–Snapin coupling. Consistently, elevated Snapin expression restores retrograde transport and enhances axonal removal of mitophagosomes, thereby reducing mitochondrial stress at AD synapses (Figs 6 and EV5A). We have shown that, while defects in Snapin-mediated retrograde transport recapitulate synaptic mitophagy stress as we observed in AD neurons, *snapin* deficiency in mouse brains leads to synaptic

degeneration (Fig 5). Moreover, Snapin-enhanced retrograde transport ameliorates synaptic loss in AD mouse brains infected with AAV-Snapin (Fig 7). Collectively, these results indicate that mitophagy-mediated quality control of synaptic mitochondria is essential for synaptic maintenance. Thus, in addition to Aβ-induced mitochondrial damage, our findings allow us to propose that AD-linked synaptic mitochondrial deficit is attributed to impaired mitochondrial maintenance at synaptic terminals due to mitophagy failure.

It is well established that proteolytically active lysosomes are highly enriched in the soma of neurons (Cai *et al*, 2010, 2012b; Gowrishankar *et al*, 2015; Xie *et al*, 2015; Maday & Holzbaur, 2016; Tammineni *et al*, 2017a; Cheng *et al*, 2018; Yap *et al*, 2018; Lee *et al*, 2019). We and others have shown that impaired lysosomal proteolysis results in lysosomal accumulation of undigested substrates, including autophagy cargoes, in the neuronal soma (Cai *et al*, 2010, 2012b; Xie *et al*, 2015; Maday & Holzbaur, 2016; Tammineni *et al*, 2017a; Cheng *et al*, 2018; Lee *et al*, 2019). Consistent with somatic localization of mature lysosomes in neurons, previous studies reported that acidic mitochondria can be detected in the soma, but not in the axons of neurons (Bingol *et al*, 2014; Puri *et al*, 2019). In the current study, our observations further support the notion that, upon mitochondrial damage, mitophagic clearance within lysosomes mainly occurs in the soma (Fig EV4A–D). Therefore, efficient retrograde transport plays a critical role in removing newly generated mitophagosomes from distal axons for lysosomal degradation in the soma, thereby reducing mitophagic stress at synaptic terminals. Lysosomal deficiency has been implicated as one of the main cell defects in AD brains (Nixon, 2013; Menzies *et al*, 2015). We found that AD neurons displayed aberrant accumulation of mitolysosomes in the soma, but not within axons in the presence or absence of $\Delta\psi_m$ dissipation (Fig EV4E–I). Our previous work revealed that Parkin-mediated mitophagy is induced in the soma of AD neurons. Moreover, lysosomal proteolysis of autophagic substrates is impaired as a result of lysosomal protease deficiency in these AD neurons (Ye *et al*, 2015; Tammineni *et al*, 2017a). Thus, mitolysosomal retention in the soma of AD neurons could be attributed to Parkin-mediated mitophagy induction and defects in lysosomal proteolysis. Therefore, our results indicate that lysosomal dysfunction has no direct impact on mitophagy regulation at synaptic terminals, further supporting the view that mitophagy stress at AD synapses is caused by increased mitophagy initiation and defective retrograde transport of mitophagosomes.

In summary, malfunctioning mitochondria not only fail to sustain synaptic activities but also augment oxidative damage and Aβ-mediated toxicity at synaptic terminals. Our study provides new insights into the mechanism of neuronal mitophagy to maintain the integrity and function of synaptic mitochondria, thereby conceptually advancing current knowledge as to how mitophagy failure and defects in mitochondrial maintenance exacerbate synaptic mitochondrial deficits and thus augment synapse damage in AD. Elucidation of this pathological mechanism has a broad neurobiological impact because mitochondrial defects, synaptic pathology, and impaired axonal transport are the defining features of AD and other major neurodegenerative diseases. Our study provides molecular and cellular target for potential therapeutic approaches aimed at enhancing mitophagy to mitigate synaptic dysfunction in AD.

Materials and Methods

Materials

pMXs-EGFP-Rheb-IP and pMXs-EGFP-Rheb SSVM-IP were from S. Yamanaka, pRK5-Myc-Rheb was from K. Guan, and Matrix-roGFP was from P. Schumacker. pLKO.1 Rheb shRNA #1, pLKO.1 Rheb shRNA #2, and pLKO.1 scrambled shRNA were from D. Sabatini. pLKO.1 Nix shRNA was from J. Gordon. pFUChW Parkin shRNA and pFUChW non-targeting shRNA were from D. Chan. pcDNA3.1 PS1L286V and PS1L286E were from X. Xu. pEBFP2-Mito-7 was from M. Davidson. Snapin and pMT-mKeima-Red plasmids and polyclonal antibody were obtained from Z.H. Sheng. The constructs encoding Snapin, Snapin-L99K, DsRed-Mito, GFP-LC3B, YFP-Rab7, YFP-Parkin, GFP-LAMP1, and AAV2/9-mCherry and AAV2/9-mCherry-Snapin constructs were prepared as previously described (Cai *et al*, 2010, 2012b; Ye & Cai, 2014; Ye *et al*, 2015, 2017; Feng *et al*, 2017; Tammineni *et al*, 2017b). Sources of antibodies and reagents are as follows: polyclonal antibodies against LC3 (Cat. 2775), Rheb (Cat. 13879), and HSP60 (Cat. 12165) (Cell Signaling Technology), p62/SQSTM1 (Cat. PM045) (MBL), SOD2 (Cat. HPA001814) (Sigma), synaptophysin (Cat. sc-9116) and TOM20 (Cat. sc-11415) (Santa Cruz), NeuN (Cat. ABN78) (Millipore/CHEMICON), Oligomer A11 (Cat. AHB0052) (Thermo Scientific); monoclonal antibodies against Rab7 (Cat. R8779) (Sigma), p62/SQSTM1 (Cat. H00008878-M01) (Abnova), Myc (Cat. #2276) (Cell Signaling Technology), HA (Cat. MMS-101P) (Covance), CI-MPR (Cat. 86f7) (Developmental Studies Hybridoma Bank), PSD95 (Cat. 05-494) (Upstate), Parkin (Cat. sc-32282) (Santa Cruz), synaptophysin (Cat. MAB5258-1) and GAPDH (Cat. CB1001) (Millipore/CHEMICON), p115 (Cat. 612261) and cytochrome *c* (Cat. 556432) (BD Biosciences), mCherry (Cat. 632543) (Clontech), VDAC (Cat. ab14734) (Abcam); β Amyloid (6E10) (Cat. SIG-39320) (BioLegend); Alexa Fluor 488 (anti-mouse: Cat. A-11017; anti-rabbit: Cat. A-11070)-, 546 (anti-mouse: Cat. A-11018; anti-rabbit: Cat. A-11071)-, and 647 (anti-mouse: Cat. A-21235; anti-rabbit: Cat. A-21246)-conjugated secondary antibodies (Invitrogen); and CCCP (Cat. 215911), Z-VAD-FMK (Cat. 219007), antimycin A (Cat. A8674), trehalose (Cat. T0167), and DMSO (Cat. 116743) (Sigma).

Mouse lines and animal care

snapin flox mice were provided by Z.H. Sheng (National Institute of Neurologic Disorders and Stroke, NIH, Bethesda, MD). CaMKIIα-tTA and tet-APPswe/ind mice were obtained from H. Cai (National Institute on Aging, NIH, Bethesda, MD). Mutant hAPPswe/ind Tg (J20) mice (C57BL/6J) (Mucke *et al*, 2000), CamKII-cre mice, and Thy1-cre Tg mice were purchased from the Jackson Laboratory and crossed with *snapin flox* mice, respectively. All animal procedures were carried out following the Rutgers Institutional Animal Care and USE COMMITTEE (IACUC). The animal facilities at Rutgers University are fully AAALAC-accredited.

Preparation of synapse-enriched fractions

Synaptosomal preparations from the brains of WT and mutant hAPP Tg mice or *snapin* conditional KO mice were collected using Percoll gradient centrifugation as described in the protocol (Leenders *et al*,

2004). Cortex tissues were homogenized in ice-cold sucrose buffer [5 mM HEPES, 1 mM EDTA, 0.32 M sucrose and protease inhibitors (Roche, Indianapolis, IN), pH 7.4]. Homogenates were centrifuged at 1,000 g for 10 min, and the supernatant was gathered and overlaid on Percoll gradients that has 2 ml of 10% Percoll gradient layered over 15, 23, and 40% Percoll gradients. The gradient was then separated by centrifugation for 5 min at 32,500 g. The synaptosomal fraction was collected from the 15%/23% Percoll layers and combined with 5 ml the sucrose buffer. The mixture was then centrifuged at 15,000 g for 15 min and resuspended in the sucrose buffer. Protein quantification was performed by BCA assay (Pierce Chemical Co./Thermo scientific). 10 µg of protein from synaptosome (Syn) and post-nuclear supernatant (PNS) homogenates were resolved by 4–12% Bis-Tris for sequential Western blots on the same membranes after stripping between each application of antibody. For multiple detection with different antibodies, blots were first stripped in a solution of 62.5 mM Tris–HCl, pH 7.5, 20 mM dithiothreitol, and 1% SDS for 15 min at 50°C with agitation and then washed with TBS/0.1% Tween-20 for 2 × 15 min (Leenders et al, 2004; Cai et al, 2010; Ye et al, 2017).

Preparation of mitochondria-enriched fractions

Mitochondria-enriched membrane was prepared as previously described (Ye et al, 2015). Briefly, WT or mutant hAPP Tg or snapin conditional KO mouse brains were homogenized in ice-cold Isolation Buffer (IB) [10 mM Tris–HCl, 1 mM EGTA, 1 mM EDTA, 0.25 M sucrose and protease inhibitors (Roche), pH7.4]. For membrane fractionation of cultured neurons, WT or mutant hAPP Tg cortical neurons were plated in 100-mm dishes at a density of 5×10^6 and treated with DMSO or 10 µM CCCP at DIV14–17. After washing once with PBS, cells were harvested and suspended in ice-cold IB Buffer. Cells were then homogenized 20 times by passing through a 25-gauge needle using a 1-ml syringe on ice. Following centrifugation of homogenates from mouse brains or cells at 1,000 g for 10 min at 4°C, the supernatant was saved as post-nuclear supernatant (P). The supernatant was further centrifuged at 15,000 g for 10 min to separate the mitochondria-enriched fraction (M) from the cytosol-enriched fraction (S). Protein concentration of mitochondria-enriched membrane fractions was determined by BCA protein assay (Pierce Chemical Co./Thermo scientific) using BSA standards. The same amount of protein (20 µg) from each fraction was resolved by 4–12% Bis-Tris PAGE for sequential Western blots on the same membranes after stripping between each application of antibody.

HEK293 and HeLa cell culture and transfection

HEK293 and HeLa cell lines (ATCC) were incubated with high glucose Dulbecco's modified Eagle's medium (DMEM) containing sodium pyruvate and L-glutamine, supplemented with 10% fetal bovine serum (FBS) and penicillin–streptomycin (Invitrogen). Lipofectamine 2000 was used for transient transfection of cells. 100 µl of Opti-MEM (Invitrogen) and 5 µl of Lipofectamine 2000 (Invitrogen) per 35 mm dish were pre-incubated at room temperature (RT) for 5 min and then mixed with 100 µl of Opti-MEM containing DNA plasmids (2–3 µg per 35 mm dish) and incubated for 20 min at RT to allow complex formation. The entire mixture was added directly to cultured cells. Following transfection, cells were cultured for an additional 1–2 days before harvesting for biochemical analysis.

Immunoprecipitation

Equal amounts of 1,000 µg cortical neuron lysates treated with CCCP or 800 µg transfected HeLa cell lysates with and without CCCP treatment were incubated with anti-Rheb antibody or anti-Myc antibody or anti-normal IgG in 200 µl of TBS with 0.1% Triton X-100, 10 mM EDTA, and protease inhibitors, and incubated on a rotator at 4°C for overnight. 2.5 mg Protein A-Sepharose CL-4B resin (GE Healthcare) was added to each sample, and the incubation continued for an additional 3 h followed by three washes with TBS with 0.1% Triton X-100. Immobilized protein complexes were processed for 4–12% Bis-Tris PAGE and immunoblotting on the same membranes after stripping between each application of the antibody.

Tissue preparation and immunohistochemistry

Animals were anesthetized with 2.5% avertin (0.35 ml per mouse) and transcardially perfused with fixation buffer (4% paraformaldehyde in PBS, pH 7.4). Brains were dissected out and post-fixed in fixation buffer overnight and then placed in 30% sucrose at 4°C. 10-µm-thick coronal sections were collected consecutively to the level of the hippocampus and used to study co-localization of various markers. After incubation with blocking buffer (5% goat serum, 0.3% Triton X-100, 3% BSA, 1% glycine in PBS) at RT for 1 h, the sections were incubated with primary antibodies at 4°C overnight, followed by incubating with secondary fluorescence antibodies at 1:600 dilution at RT for 1 h. After fluorescence immunolabeling, the sections were stained with DAPI and washed three times in PBS. The sections were then mounted with anti-fading medium (Vector Laboratories, H-5000) for imaging. Confocal images were obtained using an Olympus FV1000 oil immersion 40× objective with sequential-acquisition setting. Eight to ten sections were taken from top-to-bottom of the specimen, and brightest point projections were made.

Transmission electron microscopy

Hippocampi from WT and mutant hAPP Tg or snapin cKO mice were cut into small specimens (one dimension < 1 mm) and fixed in Trumps fixative (Electron Microscopy Sciences) for 2 h at RT. The sections were then washed by 0.1 M cacodylate buffer, and post-fixed in 1% osmium tetroxide, followed by dehydrating in ethanol, and embedding using the EM bed 812 kit (Electron Microscopy Sciences) according to a stand procedure. Images were acquired on an electron microscope (1200EX; JEOL) (Electron Imaging Facility in the Department of pathology and Laboratory Medicine, Robert Wood Johnson Medical School). For quantitative studies, the number of mitochondria and the number of mitochondria within autophagic vacuole (AV)-like organelles at presynaptic terminals were counted from electron micrographs, respectively. Mitophagosomes were characterized by mitochondria within double-membrane structures (AVi) or surrounded by structures (AVd or amphisome) containing partially degraded cytoplasmic components, vesicles, or high electron dense materials (Nixon, 2005; Cai et al, 2010; Klionsky et al, 2016; Tammineni et al, 2017b). Quantification analysis was performed blindly to condition.

Transfection of cultured cortical neurons

Cortices were dissected from E18-19 mouse embryos as described (Cai *et al*, 2010, 2012b; Ye *et al*, 2015, 2017; Tammineni *et al*, 2017b). Cortical neurons were dissociated by papain (Worthington) and plated at a density of 200,000 cells per cm^2 on polyornithine- and fibronectin-coated coverslips. Neurons were grown overnight in plating medium (5% FBS, insulin, glutamate, G5 and 1 × B27) supplemented with 100× L-glutamine in Neurobasal medium (Invitrogen). Starting at DIV2, cultures were maintained in conditioned medium with half-feed changes of neuronal feed (1 × B27 in Neurobasal medium) every 3 days. Neurons were treated with DMSO, 10 μM CCCP, 10 μM CCCP and 5 μM E64D/5 μM pepstatin A, or 1 μM antimycin A (AA) for 24 h, or transfected with various constructs at DIV5-7 using Lipofectamine 2000 (Invitrogen) followed by time-lapse imaging 10–12 days after transfection.

Image acquisition and quantification

Confocal images were obtained using an Olympus FV1000 oil immersion 60× objective with sequential-acquisition setting. For fluorescent quantification, images were acquired using the same settings below saturation at a resolution of 1,024 × 1,024 pixels (8 bit). Eight to ten sections were taken from top-to-bottom of the specimen, and brightest point projections were made. Co-localization and morphometric measurements were performed using NIH ImageJ. Measured data were imported into Excel software for analysis. The thresholds in all images were set to similar levels. Data were obtained from at least three independent experiments, and the number of cells used for quantification was indicated in the figures. All statistical analyses were performed using Student's *t*-test and are presented as mean ± SEM.

For live-cell imaging, cells were transferred to Tyrode's solution containing 10 mM HEPES, 10 mM glucose, 1.2 mM CaCl$_2$, 1.2 mM MgCl$_2$, 3 mM KCl, and 145 mM NaCl, pH 7.4. Temperature was maintained at 37°C with an air stream incubator. Cells were visualized with a 60× oil immersion lens (1.3 numerical aperture) on an Olympus FV1000 confocal microscope, using 488 nm excitation for GFP or YFP, 543 nm for DsRed, or 405 for DAPI. Time-lapse sequences of 1,024 × 1,024 pixels (8 bit) were collected at 5-s intervals with 1% intensity of the argon laser to minimize laser-induced bleaching and damage to cells, and maximum pinhole opening. Time-lapse images were captured by a total of 100 frames. All recordings started 6 min after the coverslip was placed in the chamber. The stacks of representative images were imported into NIH ImageJ. A membranous organelle was considered stopped if it remained stationary for the entire recording period; a motile one was counted only if the displacement was at least 5 μm.

For analyzing the motility of mitochondria, mitophagosomes, or mito-amphisomes in live neurons, we selected axons for time-lapse imaging and measuring motility because axons, but not dendrites, have a uniform microtubule organization and polarity. Axonal processes were selected as we previously reported (Cai *et al*, 2010, 2012b; Ye & Cai, 2014; Ye *et al*, 2015, 2017; Tammineni *et al*, 2017a,b). Briefly, axons in live images were distinguished from dendrites based on known morphological characteristics: greater length, thin and uniform diameter, and sparse branching. Only those that appeared to be single axons and separate from other processes in the field were chosen for recording axonal transport. Regions where crossing or fasciculation occurred were excluded from analysis.

Kymographs were used to trace axonal anterograde or retrograde movement of membranous organelles and to count stationary ones as described previously (Cai *et al*, 2010, 2012b; Ye & Cai, 2014; Ye *et al*, 2015, 2017; Tammineni *et al*, 2017a,b) with extra plug-ins for ImageJ (NIH). Briefly, we used the "Straighten" plugin to straighten curved axons and the "Grouped ZProjector" to *z*-axially project resliced time-lapse images. The height of the kymographs represents recording time (100 s unless otherwise noted), while the width represents the length (μm) of the axon imaged. Counts were averaged from 100 frames for each time-lapse image to ensure accuracy of stationary and motile events. Measurements are presented as mean ± SEM. Statistical analyses were performed using unpaired Student's *t*-tests.

Quantification of the density of presynaptic terminals was performed in the hippocampal mossy fiber regions using synaptophysin (SYP) fluorescence as previously reported (Mucke *et al*, 2000; Nagahara *et al*, 2013; Ye *et al*, 2017). Sampled sections consisted of 320 μm × 320 μm images acquired with an Olympus Confocal Microscope at 2,048 × 2,048 pixel resolution with a 40× objective lens. The number of pixels containing SYP immunoreactivity was measured per unit area above a minimum threshold intensity determined with the thresholding function of NIH ImageJ: Histograms of pixel brightness reflecting a bimodal distribution of background peak (mode) and a smaller signal peak (SYP fluorescence), with a 1.5 SD above background (mode), were generated. The area occupied by SYP-labeled presynaptic terminals was quantified and expressed as a percentage of the total image area as described previously (Mucke *et al*, 2000; Nagahara *et al*, 2013; Ye *et al*, 2017). To ensure objective assessments and reliability of results, brain sections from mice to be compared in any given experiment were blind-coded and processed in parallel. Codes were broken after the analysis was complete.

Determine oxidized mitochondria in live neurons

MitoROGFP (Addgene plasmid 49437) was used to measure mitochondrial oxidation in live neurons (Waypa *et al*, 2010; Xie *et al*, 2013). Neurons expressing MitoROGFP were excited at 405 nm or 488 nm with a sequential line scanning method. The emission was configured and detected at 510 nm. Images were processed using FV1000 software, ImageJ, and Adobe Photoshop CS3 (Adobe systems). To compare the intensities of the soma and axons of neurons between two excitation wavelengths (405 and 488 nm), the same ROIs were chosen to obtain intensity values for both excitation wavelengths. The 405/488 ratios in each experiment were normalized to the values of WT or mutant hAPP Tg neurons in the presence or absence of CCCP.

Determine acidic mitochondria in live neurons

Live-cell imaging was performed in WT or mutant hAPP cortical neurons expressing mt-Keima alone or mt-Keima with other different constructs after treatment with DMSO, CCCP, or CCCP with

lysosomal inhibitors (LIs) pepstatin A (5 μM) and E64D (5 μM). Neurons were visualized with an FV3000 oil immersion 60× objective with two sequential excitation lasers at 440 nm (green, healthy mitochondria at neutral pH) and 586 nm (red, damaged mitochondria engulfed by lysosomes under acidic pH) and an emission spectrum from 590 to 680 nm (Katayama *et al*, 2011; Bingol *et al*, 2014; Puri *et al*, 2019). Images were sequentially acquired from top to bottom with Z-step (0.5 μm) at a resolution of 1,024 × 1,024 pixels, 8 bit, and stacked using Z-projection (maximum intensity). Images were imported into ImageJ (NIH), and the background was removed using the built-in plugin "remove background" prior to quantification.

In *vivo* gene delivery

The AAV2/9-mCherry and AAV2/9-mCherry-Snapin constructs were kindly provided by Z.-H. Sheng and as described previously (Xie *et al*, 2015; Ye *et al*, 2017). The AAV2/9-mCherry-Snapin construct contains an IRES segment between mouse Snapin and mCherry sequences, resulting in separate expression of mouse Snapin and mCherry. The AAV2/9-mCherry and AAV2/9-mCherry-Snapin viruses were produced by Vector BioLabs. Adult mutant hAPP Tg mice at 2–3 months of age were injected into the hippocampal dentate gyrus (AP, −2 mm; L, −1.5 mm; DV, +1.75 mm) of both cerebral hemispheres according to the stereotaxic atlas of Paxinos and Franklin (2001) using 4–8 × 10^9 total viral particles per side and analyzed 5–8 months after injection.

Data availability

We have not generated data that require deposition in a public database.

Expanded View for this article is available online.

Author contributions
SH, YYJ, PS, and QC designed the project. SH, YYJ, PS, XS, and QC conducted experiments and data analysis. QC is the senior author who conceived and designed the project and wrote the manuscript.

Conflict of interest
The authors declare that they have no conflict of interest.

References

Basso AD, Mirza A, Liu G, Long BJ, Bishop WR, Kirschmeier P (2005) The farnesyl transferase inhibitor (FTI) SCH66336 (lonafarnib) inhibits Rheb farnesylation and mTOR signaling. Role in FTI enhancement of taxane and tamoxifen anti-tumor activity. *J Biol Chem* 280: 31101–31108

Bingol B, Tea JS, Phu L, Reichelt M, Bakalarski CE, Song Q, Foreman O, Kirkpatrick DS, Sheng M (2014) The mitochondrial deubiquitinase USP30 opposes parkin-mediated mitophagy. *Nature* 510: 370–375

Birsa N, Norkett R, Wauer T, Mevissen TE, Wu HC, Foltynie T, Bhatia K, Hirst WD, Komander D, Plun-Favreau H *et al* (2014) Lysine 27 ubiquitination of the mitochondrial transport protein Miro is dependent on serine 65 of the Parkin ubiquitin ligase. *J Biol Chem* 289: 14569–14582

Cai Q, Lu L, Tian JH, Zhu YB, Qiao H, Sheng ZH (2010) Snapin-regulated late endosomal transport is critical for efficient autophagy-lysosomal function in neurons. *Neuron* 68: 73–86

Cai Q, Sheng ZH (2011) Uncovering the role of Snapin in regulating autophagy-lysosomal function. *Autophagy* 7: 445–447

Cai Q, Zakaria HM, Sheng ZH (2012a) Long time-lapse imaging reveals unique features of PARK2/Parkin-mediated mitophagy in mature cortical neurons. *Autophagy* 8: 976–978

Cai Q, Zakaria HM, Simone A, Sheng ZH (2012b) Spatial parkin translocation and degradation of damaged mitochondria via mitophagy in live cortical neurons. *Curr Biol* 22: 545–552

Cai Q, Tammineni P (2016) Alterations in mitochondrial quality control in Alzheimer's disease. *Front Cell Neurosci* 10: 24

Cai Q, Tammineni P (2017) Mitochondrial aspects of synaptic dysfunction in Alzheimer's disease. *J Alzheimers Dis* 57: 1087–1103

Cai Q, Jeong YY (2020) Mitophagy in Alzheimer's disease and other age-related neurodegenerative diseases. *Cells* 9: 150

Chamberlain KA, Sheng ZH (2019) Mechanisms for the maintenance and regulation of axonal energy supply. *J Neurosci Res* 97: 897–913

Chan NC, Chan DC (2011) Parkin uses the UPS to ship off dysfunctional mitochondria. *Autophagy* 7: 771–772

Cheng XT, Zhou B, Lin MY, Cai Q, Sheng ZH (2015a) Axonal autophagosomes recruit dynein for retrograde transport through fusion with late endosomes. *J Cell Biol* 209: 377–386

Cheng XT, Zhou B, Lin MY, Cai Q, Sheng ZH (2015b) Axonal autophagosomes use the ride-on service for retrograde transport toward the soma. *Autophagy* 11: 1434–1436

Cheng XT, Xie YX, Zhou B, Huang N, Farfel-Becker T, Sheng ZH (2018) Characterization of LAMP1-labeled nondegradative lysosomal and endocytic compartments in neurons. *J Cell Biol* 217: 3127–3139

Cummins N, Tweedie A, Zuryn S, Bertran-Gonzalez J, Gotz J (2019) Disease-associated tau impairs mitophagy by inhibiting Parkin translocation to mitochondria. *EMBO J* 38: e99360

Devireddy S, Liu A, Lampe T, Hollenbeck PJ (2015) The organization of mitochondrial quality control and life cycle in the nervous system *in vivo* in the absence of PINK1. *J Neurosci* 35: 9391–9401

DiGiovanni J, Sun T, Sheng ZH (2012) Characterizing synaptic vesicle proteins using synaptosomal fractions and cultured hippocampal neurons. *Curr Protoc Neurosci* Chapter 2: Unit 2 7 1-22

Du H, Guo L, Yan S, Sosunov AA, McKhann GM, Yan SS (2010) Early deficits in synaptic mitochondria in an Alzheimer's disease mouse model. *Proc Natl Acad Sci USA* 107: 18670–18675

Du H, Guo L, Yan SS (2012) Synaptic mitochondrial pathology in Alzheimer's disease. *Antioxid Redox Signal* 16: 1467–1475

Du F, Yu Q, Yan S, Hu G, Lue LF, Walker DG, Wu L, Yan SF, Tieu K, Yan SS (2017) PINK1 signalling rescues amyloid pathology and mitochondrial dysfunction in Alzheimer's disease. *Brain* 140: 3233–3251

Fang EF, Hou Y, Palikaras K, Adriaanse BA, Kerr JS, Yang B, Lautrup S, Hasan-Olive MM, Caponio D, Dan X *et al* (2019) Mitophagy inhibits amyloid-beta and tau pathology and reverses cognitive deficits in models of Alzheimer's disease. *Nat Neurosci* 22: 401–412

Fei P, Wang W, Kim SH, Wang S, Burns TF, Sax JK, Buzzai M, Dicker DT, McKenna WG, Bernhard EJ *et al* (2004) Bnip3L is induced by p53 under hypoxia, and its knockdown promotes tumor growth. *Cancer Cell* 6: 597–609

Feng T, Tammineni P, Agrawal C, Jeong YY, Cai Q (2017) Autophagy-mediated regulation of BACE1 protein trafficking and degradation. *J Biol Chem* 292: 1679–1690

Gibson GE, Shi Q (2010) A mitocentric view of Alzheimer's disease suggests multi-faceted treatments. *J Alzheimers Dis* 20(Suppl 2): S591–S607

Gowrishankar S, Yuan P, Wu Y, Schrag M, Paradise S, Grutzendler J, De Camilli P, Ferguson SM (2015) Massive accumulation of luminal protease-deficient axonal lysosomes at Alzheimer's disease amyloid plaques. *Proc Natl Acad Sci USA* 112: E3699–E3708

Groenewoud MJ, Zwartkruis FJ (2013) Rheb and Rags come together at the lysosome to activate mTORC1. *Biochem Soc Trans* 41: 951–955

Guo L, Tian J, Du H (2017) Mitochondrial dysfunction and synaptic transmission failure in Alzheimer's disease. *J Alzheimers Dis* 57: 1071–1086

Hung COY, Livesey FJ (2018) Altered gamma-secretase processing of APP disrupts lysosome and autophagosome function in monogenic Alzheimer's disease. *Cell Rep* 25: 3647–3660 e3642

Kang C, Yeo D, Ji LL (2016) Muscle immobilization activates mitophagy and disrupts mitochondrial dynamics in mice. *Acta Physiol (Oxf)* 218: 188–197

Katayama H, Kogure T, Mizushima N, Yoshimori T, Miyawaki A (2011) A sensitive and quantitative technique for detecting autophagic events based on lysosomal delivery. *Chem Biol* 18: 1042–1052

Kim SR, Kareva T, Yarygina O, Kholodilov N, Burke RE (2012) AAV transduction of dopamine neurons with constitutively active Rheb protects from neurodegeneration and mediates axon regrowth. *Mol Ther* 20: 275–286

Klionsky DJ, Abdelmohsen K, Abe A, Abedin MJ, Abeliovich H, Acevedo Arozena A, Adachi H, Adams CM, Adams PD, Adeli K *et al* (2016) Guidelines for the use and interpretation of assays for monitoring autophagy. *Autophagy* 12: 1–222

Koentjoro B, Park JS, Sue CM (2017) Nix restores mitophagy and mitochondrial function to protect against PINK1/Parkin-related Parkinson's disease. *Sci Rep* 7: 44373

Kruger U, Wang Y, Kumar S, Mandelkow EM (2012) Autophagic degradation of tau in primary neurons and its enhancement by trehalose. *Neurobiol Aging* 33: 2291–2305

Kulic L, Walter J, Multhaup G, Teplow DB, Baumeister R, Romig H, Capell A, Steiner H, Haass C (2000) Separation of presenilin function in amyloid beta-peptide generation and endoproteolysis of Notch. *Proc Natl Acad Sci USA* 97: 5913–5918

Lee JH, Yu WH, Kumar A, Lee S, Mohan PS, Peterhoff CM, Wolfe DM, Martinez-Vicente M, Massey AC, Sovak G *et al* (2010) Lysosomal proteolysis and autophagy require presenilin 1 and are disrupted by Alzheimer-related PS1 mutations. *Cell* 141: 1146–1158

Lee JH, Rao MV, Yang DS, Stavrides P, Im E, Pensalfini A, Huo C, Sarkar P, Yoshimori T, Nixon RA (2019) Transgenic expression of a ratiometric autophagy probe specifically in neurons enables the interrogation of brain autophagy *in vivo*. *Autophagy* 15: 543–557

Leenders M, Gerwin C, Sheng ZH (2004) Multidisciplinary approaches for characterizing synaptic vesicle proteins. *Curr Protoc Neurosci* Chapter 2: Unit 2 7

Lin MY, Cheng XT, Tammineni P, Xie Y, Zhou B, Cai Q, Sheng ZH (2017) Releasing syntaphilin removes stressed mitochondria from axons independent of mitophagy under pathophysiological conditions. *Neuron* 94: 595–610 e596

Liu S, Sawada T, Lee S, Yu W, Silverio G, Alapatt P, Millan I, Shen A, Saxton W, Kanao T *et al* (2012) Parkinson's disease-associated kinase PINK1 regulates Miro protein level and axonal transport of mitochondria. *PLoS Genet* 8: e1002537

Maday S, Wallace KE, Holzbaur EL (2012) Autophagosomes initiate distally and mature during transport toward the cell soma in primary neurons. *J Cell Biol* 196: 407–417

Maday S, Holzbaur EL (2016) Compartment-specific regulation of autophagy in primary neurons. *J Neurosci* 36: 5933–5945

Manczak M, Kandimalla R, Yin X, Reddy PH (2018) Hippocampal mutant APP and amyloid beta-induced cognitive decline, dendritic spine loss, defective autophagy, mitophagy and mitochondrial abnormalities in a mouse model of Alzheimer's disease. *Hum Mol Genet* 27: 1332–1342

Manji H, Kato T, Di Prospero NA, Ness S, Beal MF, Krams M, Chen G (2012) Impaired mitochondrial function in psychiatric disorders. *Nat Rev Neurosci* 13: 293–307

Manning BD, Cantley LC (2003) United at last: the tuberous sclerosis complex gene products connect the phosphoinositide 3-kinase/Akt pathway to mammalian target of rapamycin (mTOR) signalling. *Biochem Soc Trans* 31: 573–578

Melser S, Chatelain EH, Lavie J, Mahfouf W, Jose C, Obre E, Goorden S, Priault M, Elgersma Y, Rezvani HR *et al* (2013) Rheb regulates mitophagy induced by mitochondrial energetic status. *Cell Metab* 17: 719–730

Melser S, Lavie J, Benard G (2015) Mitochondrial degradation and energy metabolism. *Biochim Biophys Acta* 1853: 2812–2821

Menzies FM, Fleming A, Rubinsztein DC (2015) Compromised autophagy and neurodegenerative diseases. *Nat Rev Neurosci* 16: 345–357

Moreira PI, Siedlak SL, Wang X, Santos MS, Oliveira CR, Tabaton M, Nunomura A, Szweda LI, Aliev G, Smith MA *et al* (2007a) Autophagocytosis of mitochondria is prominent in Alzheimer disease. *J Neuropathol Exp Neurol* 66: 525–532

Moreira PI, Siedlak SL, Wang X, Santos MS, Oliveira CR, Tabaton M, Nunomura A, Szweda LI, Aliev G, Smith MA *et al* (2007b) Increased autophagic degradation of mitochondria in Alzheimer disease. *Autophagy* 3: 614–615

Mucke L, Masliah E, Yu GQ, Mallory M, Rockenstein EM, Tatsuno G, Hu K, Kholodenko D, Johnson-Wood K, McConlogue L (2000) High-level neuronal expression of abeta 1-42 in wild-type human amyloid protein precursor transgenic mice: synaptotoxicity without plaque formation. *J Neurosci* 20: 4050–4058

Nagahara AH, Merrill DA, Coppola G, Tsukada S, Schroeder BE, Shaked GM, Wang L, Blesch A, Kim A, Conner JM *et al* (2009) Neuroprotective effects of brain-derived neurotrophic factor in rodent and primate models of Alzheimer's disease. *Nat Med* 15: 331–337

Nagahara AH, Mateling M, Kovacs I, Wang L, Eggert S, Rockenstein E, Koo EH, Masliah E, Tuszynski MH (2013) Early BDNF treatment ameliorates cell loss in the entorhinal cortex of APP transgenic mice. *J Neurosci* 33: 15596–15602

Neely Kayala KM, Dickinson GD, Minassian A, Walls KC, Green KN, Laferla FM (2012) Presenilin-null cells have altered two-pore calcium channel expression and lysosomal calcium: implications for lysosomal function. *Brain Res* 1489: 8–16

Nixon RA (2005) Endosome function and dysfunction in Alzheimer's disease and other neurodegenerative diseases. *Neurobiol Aging* 26: 373–382

Nixon RA (2013) The role of autophagy in neurodegenerative disease. *Nat Med* 19: 983–997

Nnah IC, Wang B, Saqcena C, Weber GF, Bonder EM, Bagley D, De Cegli R, Napolitano G, Medina DL, Ballabio A *et al* (2019) TFEB-driven endocytosis coordinates MTORC1 signaling and autophagy. *Autophagy* 15: 151–164

Paxinos G, Franklin KBJ (2001) *The mouse brain in stereotaxic coordinates*, 2nd edn. San Diego, CA: Academic Press

Pickles S, Vigie P, Youle RJ (2018) Mitophagy and quality control mechanisms in mitochondrial maintenance. *Curr Biol* 28: R170–R185

Pickrell AM, Youle RJ (2015) The roles of PINK1, parkin, and mitochondrial fidelity in Parkinson's disease. *Neuron* 85: 257–273

Polito VA, Li H, Martini-Stoica H, Wang B, Yang L, Xu Y, Swartzlander DB, Palmieri M, di Ronza A, Lee VM *et al* (2014) Selective clearance of aberrant tau proteins and rescue of neurotoxicity by transcription factor EB. *EMBO Mol Med* 6: 1142–1160

Puri R, Cheng XT, Lin MY, Huang N, Sheng ZH (2019) Mul1 restrains Parkin-mediated mitophagy in mature neurons by maintaining ER-mitochondrial contacts. *Nat Commun* 10: 3645

Reddy PH, Beal MF (2008) Amyloid beta, mitochondrial dysfunction and synaptic damage: implications for cognitive decline in aging and Alzheimer's disease. *Trends Mol Med* 14: 45–53

Reddy PH, Manczak M, Mao P, Calkins MJ, Reddy AP, Shirendeb U (2010) Amyloid-beta and mitochondria in aging and Alzheimer's disease: implications for synaptic damage and cognitive decline. *J Alzheimers Dis* 20 (Suppl 2): S499–S512

Reddy PH (2011) Abnormal tau, mitochondrial dysfunction, impaired axonal transport of mitochondria, and synaptic deprivation in Alzheimer's disease. *Brain Res* 1415: 136–148

Reddy PH, Yin X, Manczak M, Kumar S, Pradeepkiran JA, Vijayan M, Reddy AP (2018) Mutant APP and amyloid beta-induced defective autophagy, mitophagy, mitochondrial structural and functional changes and synaptic damage in hippocampal neurons from Alzheimer's disease. *Hum Mol Genet* 27: 2502–2516

Reddy PH, Oliver DM (2019) Amyloid beta and phosphorylated tau-induced defective autophagy and mitophagy in Alzheimer's disease. *Cells* 8: 488

Rojansky R, Cha MY, Chan DC (2016) Elimination of paternal mitochondria in mouse embryos occurs through autophagic degradation dependent on PARKIN and MUL1. *Elife* 5: e17896

Sepuri NBV, Tammineni P, Mohammed F, Paripati A (2017) Nuclear transcription factors in the mitochondria: a new paradigm in fine-tuning mitochondrial metabolism. *Handb Exp Pharmacol* 240: 3–20

Shahani N, Pryor W, Swarnkar S, Kholodilov N, Thinakaran G, Burke RE, Subramaniam S (2014) Rheb GTPase regulates beta-secretase levels and amyloid beta generation. *J Biol Chem* 289: 5799–5808

Shahani N, Huang WC, Varnum M, Page DT, Subramaniam S (2017) Forebrain depletion of Rheb GTPase elicits spatial memory deficits in mice. *Neurobiol Aging* 50: 134–143

Sheng ZH, Cai Q (2012) Mitochondrial transport in neurons: impact on synaptic homeostasis and neurodegeneration. *Nat Rev Neurosci* 13: 77–93

Sung H, Tandarich LC, Nguyen K, Hollenbeck PJ (2016) Compartmentalized regulation of Parkin-mediated mitochondrial quality control in the drosophila nervous system *in vivo*. *J Neurosci* 36: 7375–7391

Swerdlow RH, Burns JM, Khan SM (2010) The Alzheimer's disease mitochondrial cascade hypothesis. *J Alzheimers Dis* 20(Suppl 2): S265–S279

Tammineni P, Cai Q (2017) Defective retrograde transport impairs autophagic clearance in Alzheimer disease neurons. *Autophagy* 13: 982–984

Tammineni P, Jeong YY, Feng T, Aikal D, Cai Q (2017a) Impaired axonal retrograde trafficking of the retromer complex augments lysosomal deficits in Alzheimer's disease neurons. *Hum Mol Genet* 26: 4352–4366

Tammineni P, Ye X, Feng T, Aikal D, Cai Q (2017b) Impaired retrograde transport of axonal autophagosomes contributes to autophagic stress in Alzheimer's disease neurons. *Elife* 6: e21776

Tonnies E, Trushina E (2017) Oxidative stress, synaptic dysfunction, and Alzheimer's disease. *J Alzheimers Dis* 57: 1105–1121

Tyagi R, Shahani N, Gorgen L, Ferretti M, Pryor W, Chen PY, Swarnkar S, Worley PF, Karbstein K, Snyder SH *et al* (2015) Rheb inhibits protein synthesis by activating the PERK-eIF2alpha signaling cascade. *Cell Rep* 10: 684–693

Wang X, Winter D, Ashrafi G, Schlehe J, Wong YL, Selkoe D, Rice S, Steen J, LaVoie MJ, Schwarz TL (2011) PINK1 and Parkin target Miro for phosphorylation and degradation to arrest mitochondrial motility. *Cell* 147: 893–906

Waypa GB, Marks JD, Guzy R, Mungai PT, Schriewer J, Dokic D, Schumacker PT (2010) Hypoxia triggers subcellular compartment redox signaling in vascular smooth muscle cells. *Circ Res* 106: 526–535

Winckler B, Faundez V, Maday S, Cai Q, Guimas Almeida C, Zhang H (2018) The endolysosomal system and proteostasis: from development to degeneration. *J Neurosci* 38: 9364–9374

Wong YC, Holzbaur EL (2014) The regulation of autophagosome dynamics by huntingtin and HAP1 is disrupted by expression of mutant huntingtin, leading to defective cargo degradation. *J Neurosci* 34: 1293–1305

Xiao Q, Yan P, Ma X, Liu H, Perez R, Zhu A, Gonzales E, Tripoli DL, Czerniewski L, Ballabio A *et al* (2015) Neuronal-targeted TFEB accelerates lysosomal degradation of APP, reducing abeta generation and amyloid plaque pathogenesis. *J Neurosci* 35: 12137–12151

Xie H, Guan J, Borrelli LA, Xu J, Serrano-Pozo A, Bacskai BJ (2013) Mitochondrial alterations near amyloid plaques in an Alzheimer's disease mouse model. *J Neurosci* 33: 17042–17051

Xie Y, Zhou B, Lin MY, Wang S, Foust KD, Sheng ZH (2015) Endolysosomal deficits augment mitochondria pathology in spinal motor neurons of asymptomatic fALS mice. *Neuron* 87: 355–370

Yang S, Xia C, Li S, Du L, Zhang L, Zhou R (2014) Defective mitophagy driven by dysregulation of rheb and KIF5B contributes to mitochondrial reactive oxygen species (ROS)-induced nod-like receptor 3 (NLRP3) dependent proinflammatory response and aggravates lipotoxicity. *Redox Biol* 3: 63–71

Yap CC, Digilio L, McMahon LP, Garcia ADR, Winckler B (2018) Degradation of dendritic cargos requires Rab7-dependent transport to somatic lysosomes. *J Cell Biol* 217: 3141–3159

Ye X, Cai Q (2014) Snapin-mediated BACE1 retrograde transport is essential for its degradation in lysosomes and regulation of APP processing in neurons. *Cell Rep* 6: 24–31

Ye X, Sun X, Starovoytov V, Cai Q (2015) Parkin-mediated mitophagy in mutant hAPP neurons and Alzheimer's disease patient brains. *Hum Mol Genet* 24: 2938–2951

Ye X, Feng T, Tammineni P, Chang Q, Jeong YY, Margolis DJ, Cai H, Kusnecov A, Cai Q (2017) Regulation of synaptic amyloid-beta generation through BACE1 retrograde transport in a mouse model of Alzheimer's disease. *J Neurosci* 37: 2639–2655

Youle RJ, Narendra DP (2011) Mechanisms of mitophagy. *Nat Rev Mol Cell Biol* 12: 9–14

Zhang X, Garbett K, Veeraraghavalu K, Wilburn B, Gilmore R, Mirnics K, Sisodia SS (2012) A role for presenilins in autophagy revisited: normal acidification of lysosomes in cells lacking PSEN1 and PSEN2. *J Neurosci* 32: 8633–8648